

Measurement of the Diffractive Cross Section in Deep Inelastic Scattering using ZEUS 1994 Data

ZEUS Collaboration

Abstract

The DIS diffractive cross section, $d\sigma_{\gamma^*p \rightarrow XN}^{diff}/dM_X$, has been measured in the mass range $M_X < 15$ GeV for γ^*p c.m. energies $60 < W < 200$ GeV and photon virtualities $Q^2 = 7$ to 140 GeV². For fixed Q^2 and M_X , the diffractive cross section rises rapidly with W , $d\sigma_{\gamma^*p \rightarrow XN}^{diff}(M_X, W, Q^2)/dM_X \propto W^{a^{diff}}$ with $a^{diff} = 0.507 \pm 0.034(stat)_{-0.046}^{+0.155}(syst)$ corresponding to a t -averaged pomeron trajectory of $\overline{\alpha_P} = 1.127 \pm 0.009(stat)_{-0.012}^{+0.039}(syst)$ which is larger than $\overline{\alpha_P}$ observed in hadron-hadron scattering. The W dependence of the diffractive cross section is found to be the same as that of the total cross section for scattering of virtual photons on protons. The data are consistent with the assumption that the diffractive structure function $F_2^{D(3)}$ factorizes according to $x_P F_2^{D(3)}(x_P, \beta, Q^2) = (x_0/x_P)^n F_2^{D(2)}(\beta, Q^2)$. They are also consistent with QCD based models which incorporate factorization breaking. The rise of $x_P F_2^{D(3)}$ with decreasing x_P and the weak dependence of $F_2^{D(2)}$ on Q^2 suggest a substantial contribution from partonic interactions.

The ZEUS Collaboration

J. Breitweg, M. Derrick, D. Krakauer, S. Magill, D. Mikunas, B. Musgrave, J. Repond, R. Stanek, R.L. Talaga, R. Yoshida, H. Zhang

Argonne National Laboratory, Argonne, IL, USA ^p

M.C.K. Mattingly

Andrews University, Berrien Springs, MI, USA

F. Anselmo, P. Antonioli, G. Bari, M. Basile, L. Bellagamba, D. Boscherini, A. Bruni, G. Bruni, G. Cara Romeo, G. Castellini¹, L. Cifarelli², F. Cindolo, A. Contin, N. Coppola, M. Corradi, S. De Pasquale, P. Giusti, G. Iacobucci, G. Laurenti, G. Levi, A. Margotti, T. Massam, R. Nania, F. Palmonari, A. Pesci, A. Polini, G. Sartorelli, Y. Zamora Garcia³, A. Zichichi

University and INFN Bologna, Bologna, Italy ^f

C. Amelung, A. Bornheim, I. Brock, K. Coböken, J. Crittenden, R. Deffner, M. Eckert, M. Grothe⁴, H. Hartmann, K. Heinloth, L. Heinz, E. Hilger, H.-P. Jakob, A. Kappes, U.F. Katz, R. Kerger, E. Paul, M. Pfeiffer, H. Schnurbusch, H. Wieber

Physikalisches Institut der Universität Bonn, Bonn, Germany ^c

D.S. Bailey, S. Campbell-Robson, W.N. Cottingham, B. Foster, R. Hall-Wilton, G.P. Heath, H.F. Heath, J.D. McFall, D. Piccioni, D.G. Roff, R.J. Tapper

H.H. Wills Physics Laboratory, University of Bristol, Bristol, U.K. ^o

M. Capua, L. Iannotti, A. Mastroberardino, M. Schioppa, G. Susinno

Calabria University, Physics Dept.and INFN, Cosenza, Italy ^f

J.Y. Kim, J.H. Lee, I.T. Lim, M.Y. Pac⁵

Chonnam National University, Kwangju, Korea ^h

A. Caldwell⁶, N. Cartiglia, Z. Jing, W. Liu, B. Mellado, J.A. Parsons, S. Ritz⁷, S. Sampson, F. Sciulli, P.B. Straub, Q. Zhu

Columbia University, Nevis Labs., Irvington on Hudson, N.Y., USA ^q

P. Borzemeski, J. Chwastowski, A. Eskreys, J. Figiel, K. Klimek, M.B. Przybycień, L. Zawiejski

Inst. of Nuclear Physics, Cracow, Poland ^j

L. Adamczyk⁸, B. Bednarek, M. Bukowy, A.M. Czermak, K. Jeleń, D. Kisielewska, T. Kowalski,

M. Przybycień, E. Rulikowska-Zarebska, L. Suszycki, J. Zając

Faculty of Physics and Nuclear Techniques, Academy of Mining and Metallurgy, Cracow, Poland ^j

Z. Duliński, A. Kotański

Jagellonian Univ., Dept. of Physics, Cracow, Poland ^k

G. Abbiendi⁹, L.A.T. Bauerdick, U. Behrens, H. Beier¹⁰, J.K. Bienlein, K. Desler, G. Drews, U. Fricke, I. Gialas¹¹, F. Goebel, P. Göttlicher, R. Graciani, T. Haas, W. Hain, G.F. Hartner, D. Hasell¹², K. Hebbel, K.F. Johnson¹³, M. Kasemann, W. Koch, U. Kötz, H. Kowalski, L. Lindemann, B. Löhr, M. Martínez, J. Milewski, M. Milite, T. Monteiro¹⁴, D. Notz, A. Pellegrino, F. Pelucchi, K. Piotrkowski, M. Rohde, J. Roldán¹⁵, J.J. Ryan¹⁶, P.R.B. Saull, A.A. Savin, U. Schneekloth, O. Schwarzer, F. Selonke, S. Stonjek, B. Surrow¹⁷, E. Tassi, D. Westphal¹⁸, G. Wolf, U. Wollmer, C. Youngman, W. Zeuner

Deutsches Elektronen-Synchrotron DESY, Hamburg, Germany

B.D. Burow, C. Coldewey, H.J. Grabosch, A. Meyer, S. Schlenstedt
DESY-IfH Zeuthen, Zeuthen, Germany

G. Barbagli, E. Gallo, P. Pelfer
University and INFN, Florence, Italy^f

G. Maccarrone, L. Votano
INFN, Laboratori Nazionali di Frascati, Frascati, Italy^f

A. Bamberger, S. Eisenhardt, P. Markun, H. Raach, T. Trefzger¹⁹, S. Wölffe
Fakultät für Physik der Universität Freiburg i.Br., Freiburg i.Br., Germany^c

J.T. Bromley, N.H. Brook, P.J. Bussey, A.T. Doyle²⁰, S.W. Lee, N. Macdonald, G.J. McCance,
D.H. Saxon,
L.E. Sinclair, I.O. Skillicorn, E. Strickland, R. Waugh
Dept. of Physics and Astronomy, University of Glasgow, Glasgow, U.K.^o

I. Bohnet, N. Gendner, U. Holm, A. Meyer-Larsen, H. Salehi, K. Wick
Hamburg University, I. Institute of Exp. Physics, Hamburg, Germany^c

A. Garfagnini, L.K. Gladilin²¹, D. Kçira²², R. Klanner, E. Lohrmann, G. Poelz, F. Zetsche
Hamburg University, II. Institute of Exp. Physics, Hamburg, Germany^c

T.C. Bacon, I. Butterworth, J.E. Cole, G. Howell, L. Lamberti²³, K.R. Long, D.B. Miller,
N. Pavel, A. Prinions²⁴, J.K. Sedgbeer, D. Sideris, R. Walker
Imperial College London, High Energy Nuclear Physics Group, London, U.K.^o

U. Mallik, S.M. Wang, J.T. Wu²⁵
University of Iowa, Physics and Astronomy Dept., Iowa City, USA^p

P. Cloth, D. Filges
Forschungszentrum Jülich, Institut für Kernphysik, Jülich, Germany

J.I. Fleck¹⁷, T. Ishii, M. Kuze, I. Suzuki²⁶, K. Tokushuku, S. Yamada, K. Yamauchi, Y. Yamazaki²⁷
Institute of Particle and Nuclear Studies, KEK, Tsukuba, Japan^g

S.J. Hong, S.B. Lee, S.W. Nam²⁸, S.K. Park
Korea University, Seoul, Korea^h

H. Lim, I.H. Park, D. Son
Kyungpook National University, Taegu, Korea^h

F. Barreiro, J.P. Fernández, G. García, C. Glasman²⁹, J.M. Hernández, L. Hervás¹⁷, L. Labarga,
J. del Peso, J. Puga, J. Terrón, J.F. de Trocóniz
Univer. Autónoma Madrid, Depto de Física Teórica, Madrid, Spainⁿ

F. Corriveau, D.S. Hanna, J. Hartmann, W.N. Murray, A. Ochs, M. Riveline, D.G. Stairs,
M. St-Laurent
McGill University, Dept. of Physics, Montréal, Québec, Canada^{a, b}

T. Tsurugai
Meiji Gakuin University, Faculty of General Education, Yokohama, Japan

V. Bashkirov, B.A. Dolgoshein, A. Stifutkin

Moscow Engineering Physics Institute, Moscow, Russia^l

G.L. Bashindzhagyan, P.F. Ermolov, Yu.A. Golubkov, L.A. Khein, N.A. Korotkova, I.A. Korzhavina, V.A. Kuzmin, O.Yu. Lukina, A.S. Proskuryakov, L.M. Shcheglova³⁰, A.N. Solomin³⁰, S.A. Zotkin

Moscow State University, Institute of Nuclear Physics, Moscow, Russia^m

C. Bokel, M. Botje, N. Brümmer, J. Engelen, E. Koffeman, P. Kooijman, A. van Sighem, H. Tiecke, N. Tuning, W. Verkerke, J. Vossebeld, L. Wiggers, E. de Wolf

*NIKHEF and University of Amsterdam, Amsterdam, Netherlands*ⁱ

D. Acosta³¹, B. Bylsma, L.S. Durkin, J. Gilmore, C.M. Ginsburg, C.L. Kim, T.Y. Ling, P. Nylander, T.A. Romanowski³²

Ohio State University, Physics Department, Columbus, Ohio, USA^p

H.E. Blaikley, R.J. Cashmore, A.M. Cooper-Sarkar, R.C.E. Devenish, J.K. Edmonds, J. Große-Knetter³³, N. Harnew, C. Nath, V.A. Noyes³⁴, A. Quadt, O. Ruske, J.R. Tickner³⁵, R. Walczak, D.S. Waters

Department of Physics, University of Oxford, Oxford, U.K.^o

A. Bertolin, R. Brugnera, R. Carlin, F. Dal Corso, U. Dosselli, S. Limentani, M. Morandin, M. Posocco, L. Stanco, R. Stroili, C. Voci

Dipartimento di Fisica dell'Università and INFN, Padova, Italy^f

B.Y. Oh, J.R. Okrasinski, W.S. Toothacker, J.J. Whitmore

Pennsylvania State University, Dept. of Physics, University Park, PA, USA^q

Y. Iga

Polytechnic University, Sagamihara, Japan^g

G. D'Agostini, G. Marini, A. Nigro, M. Raso

Dipartimento di Fisica, Univ. 'La Sapienza' and INFN, Rome, Italy^f

J.C. Hart, N.A. McCubbin, T.P. Shah

Rutherford Appleton Laboratory, Chilton, Didcot, Oxon, U.K.^o

D. Epperson, C. Heusch, J.T. Rahn, H.F.-W. Sadrozinski, A. Seiden, R. Wichmann, D.C. Williams
University of California, Santa Cruz, CA, USA^p

H. Abramowicz³⁶, G. Briskin³⁷, S. Dagan³⁸, S. Kananov³⁸, A. Levy³⁸

Raymond and Beverly Sackler Faculty of Exact Sciences, School of Physics, Tel-Aviv University, Tel-Aviv, Israel^e

T. Abe, T. Fusayasu, M. Inuzuka, K. Nagano, K. Umemori, T. Yamashita

Department of Physics, University of Tokyo, Tokyo, Japan^g

R. Hamatsu, T. Hirose, K. Homma³⁹, S. Kitamura⁴⁰, T. Matsushita, T. Nishimura

Tokyo Metropolitan University, Dept. of Physics, Tokyo, Japan^g

M. Arneodo²⁰, R. Cirio, M. Costa, M.I. Ferrero, S. Maselli, V. Monaco, C. Peroni, M.C. Petrucci, M. Ruspa, R. Sacchi, A. Solano, A. Staiano

Università di Torino, Dipartimento di Fisica Sperimentale and INFN, Torino, Italy^f

M. Dardo

II Faculty of Sciences, Torino University and INFN - Alessandria, Italy^f

D.C. Bailey, C.-P. Fagerstroem, R. Galea, K.K. Joo, G.M. Levman, J.F. Martin R.S. Orr, S. Polenz, A. Sabetfakhri, D. Simmons

University of Toronto, Dept. of Physics, Toronto, Ont., Canada^a

J.M. Butterworth, C.D. Catterall, M.E. Hayes, E.A. Heaphy, T.W. Jones, J.B. Lane, R.L. Saunders, M.R. Sutton, M. Wing

University College London, Physics and Astronomy Dept., London, U.K.^o

J. Ciborowski, G. Grzelak⁴¹, R.J. Nowak, J.M. Pawlak, R. Pawlak, B. Smalska, T. Tymieniecka, A.K. Wróblewski, J.A. Zakrzewski, A.F. Żarnecki

Warsaw University, Institute of Experimental Physics, Warsaw, Poland^j

M. Adamus

Institute for Nuclear Studies, Warsaw, Poland^j

O. Deppe, Y. Eisenberg³⁸, D. Hochman, U. Karshon³⁸

Weizmann Institute, Department of Particle Physics, Rehovot, Israel^d

W.F. Badgett, D. Chapin, R. Cross, S. Dasu, C. Foudas, R.J. Loveless, S. Mattingly, D.D. Reeder, W.H. Smith, A. Vaiciulis, M. Wodarczyk

University of Wisconsin, Dept. of Physics, Madison, WI, USA^p

A. Deshpande, S. Dhawan, V.W. Hughes

Yale University, Department of Physics, New Haven, CT, USA^p

S. Bhadra, W.R. Frisken, M. Khakzad, W.B. Schmidke

York University, Dept. of Physics, North York, Ont., Canada^a

¹ also at IROE Florence, Italy
² now at Univ. of Salerno and INFN Napoli, Italy
³ supported by Worldlab, Lausanne, Switzerland
⁴ now at University of California, Santa Cruz, USA
⁵ now at Dongshin University, Naju, Korea
⁶ also at DESY
⁷ Alfred P. Sloan Foundation Fellow
⁸ supported by the Polish State Committee for Scientific Research, grant No. 2P03B14912
⁹ now at INFN Bologna
¹⁰ now at Innosoft, Munich, Germany
¹¹ now at Univ. of Crete, Greece, partially supported by DAAD, Bonn - Kz. A/98/16764
¹² now at Massachusetts Institute of Technology, Cambridge, MA, USA
¹³ visitor from Florida State University
¹⁴ supported by European Community Program PRAXIS XXI
¹⁵ now at IFIC, Valencia, Spain
¹⁶ now a self-employed consultant
¹⁷ now at CERN
¹⁸ now at Bayer A.G., Leverkusen, Germany
¹⁹ now at ATLAS Collaboration, Univ. of Munich
²⁰ also at DESY and Alexander von Humboldt Fellow at University of Hamburg
²¹ on leave from MSU, supported by the GIF, contract I-0444-176.07/95
²² supported by DAAD, Bonn - Kz. A/98/12712
²³ supported by an EC fellowship
²⁴ PPARC Post-doctoral fellow
²⁵ now at Applied Materials Inc., Santa Clara
²⁶ now at Osaka Univ., Osaka, Japan
²⁷ supported by JSPS Postdoctoral Fellowships for Research Abroad
²⁸ now at Wayne State University, Detroit
²⁹ supported by an EC fellowship number ERBFMBICT 972523
³⁰ partially supported by the Foundation for German-Russian Collaboration DFG-RFBR
(grant no. 436 RUS 113/248/3 and no. 436 RUS 113/248/2)
³¹ now at University of Florida, Gainesville, FL, USA
³² now at Department of Energy, Washington
³³ supported by the Feodor Lynen Program of the Alexander von Humboldt foundation
³⁴ Glasstone Fellow
³⁵ now at CSIRO, Lucas Heights, Sydney, Australia
³⁶ an Alexander von Humboldt Fellow at University of Hamburg
³⁷ now at Brown University, Providence, RI, USA
³⁸ supported by a MINERVA Fellowship
³⁹ now at ICEPP, Univ. of Tokyo, Tokyo, Japan
⁴⁰ present address: Tokyo Metropolitan College of Allied Medical Sciences, Tokyo 116, Japan
⁴¹ supported by the Polish State Committee for Scientific Research, grant No. 2P03B09308

- ^a supported by the Natural Sciences and Engineering Research Council of Canada (NSERC)
- ^b supported by the FCAR of Québec, Canada
- ^c supported by the German Federal Ministry for Education and Science, Research and Technology (BMBF), under contract numbers 057BN19P, 057FR19P, 057HH19P, 057HH29P
- ^d supported by the MINERVA Gesellschaft für Forschung GmbH, the German Israeli Foundation, the U.S.-Israel Binational Science Foundation, and by the Israel Ministry of Science
- ^e supported by the German-Israeli Foundation, the Israel Science Foundation, the U.S.-Israel Binational Science Foundation, and by the Israel Ministry of Science
- ^f supported by the Italian National Institute for Nuclear Physics (INFN)
- ^g supported by the Japanese Ministry of Education, Science and Culture (the Monbusho) and its grants for Scientific Research
- ^h supported by the Korean Ministry of Education and Korea Science and Engineering Foundation
- ⁱ supported by the Netherlands Foundation for Research on Matter (FOM)
- ^j supported by the Polish State Committee for Scientific Research, grant No. 115/E-343/SPUB/P03/002/97, 2P03B10512, 2P03B10612, 2P03B14212, 2P03B10412
- ^k supported by the Polish State Committee for Scientific Research (grant No. 2P03B08614) and Foundation for Polish-German Collaboration
- ^l partially supported by the German Federal Ministry for Education and Science, Research and Technology (BMBF)
- ^m supported by the Fund for Fundamental Research of Russian Ministry for Science and Education and by the German Federal Ministry for Education and Science, Research and Technology (BMBF)
- ⁿ supported by the Spanish Ministry of Education and Science through funds provided by CICYT
- ^o supported by the Particle Physics and Astronomy Research Council
- ^p supported by the US Department of Energy
- ^q supported by the US National Science Foundation

1 Introduction

Diffraction has been studied extensively in hadron-hadron scattering at small momentum transfers [1]. An elegant parametrization of the data has been provided by the Regge formalism through the introduction of a pomeron trajectory [2] - [5]. The hypothesis that diffraction may have a partonic component [6] has been substantiated by the observation of a high transverse energy jet production in diffractive $p\bar{p}$ scattering [7]. However, in hadron-hadron scattering both collision partners are extended objects which makes the extraction of the underlying partonic process(es) difficult. In deep-inelastic electron-proton scattering (DIS), on the other hand, the virtual photon has a pointlike coupling to quarks. The ep collider HERA offers a unique opportunity to study the partonic structure of diffraction since it gives access to the regime of large photon virtualities Q^2 ($Q^2 = 10 - 1000 \text{ GeV}^2$) and large energy transfers between the virtual photon and the target proton in its rest system, $\nu = Q^2/(2m_p x) = 2 - 20 \text{ TeV}$, where x is the Bjorken scaling variable and m_p is the proton mass.

The diffractive dissociation of the virtual photon, first recognized by the presence of a class of events with a large rapidity gap [8, 9], has opened a window for a systematic study of diffraction in reactions initiated by a hard probe [10] - [15].

In this paper, we present a measurement of the diffractive cross section for

$$\gamma^*p \rightarrow XN \quad (1)$$

and of the diffractive structure function $F_2^{D(3)}$ [16]. Here, X and N are the particle systems produced by dissociation of the virtual photon and the proton. The measurements show that diffraction constitutes a substantial fraction of the total cross section. The latter is directly related to the proton structure function $F_2(x, Q^2)$. The principal signatures for a partonic behaviour in DIS at small x were found to be a logarithmic dependence of F_2 on Q^2 associated with a rapid rise as x decreases [17, 18, 19]. The comparison of $F_2^{D(3)}$ with $F_2(x, Q^2)$ allows a direct comparison of the QCD evolution of the two processes with respect to x and Q^2 .

In QCD, diffraction is characterized by the exchange of a colourless object, e.g. a colour singlet two-gluon system, between the incoming virtual photon and proton. The exchange of a colourless system suppresses QCD radiation, and therefore the production of hadrons, in comparison with nondiffractive scattering. In the diffractive events studied in this analysis most of the hadronic energy is carried away by a low mass nucleonic system N which escapes detection. This property is used to identify the diffractive contribution. The diffractive cross section is determined using the M_X method developed previously to separate the diffractive and nondiffractive contributions [13].

The present measurement is based on a fivefold larger data sample in a wider range in Q^2 (7 - 140 GeV^2) compared to our previous studies [11, 13]. The squared momentum transfer t from the virtual photon to the incoming proton is not measured, so the diffractive contribution was integrated over this variable. The system N is either a proton or a nucleonic system with mass $M_N < 5.5 \text{ GeV}$. The new results supersede those presented in [13] which were affected by a technical error simulating the QED radiative corrections in the Monte Carlo generation used for unfolding. This led to a steeper energy dependence and a higher intercept of the pomeron trajectory by about one unit of the quoted error.

2 Kinematics

The kinematic quantities used for the description of inclusive DIS, $e(k) + p(P) \rightarrow e(k') + \text{anything}$, are $Q^2 = -q^2 = -(k - k')^2$, $x = Q^2/(2P \cdot q)$, $y = (P \cdot q)/(P \cdot k)$ and $W^2 = Q^2(1 - x)/x + m_p^2 \approx Q^2/x$ for $x \ll 1$. Here k, k' are the four-momenta of the initial and final state positrons; P is the four-momentum of the initial state proton and y is the fractional energy transfer to the proton in its rest frame. For the range of Q^2 and W considered in this paper $W^2 \approx ys$, where $s = 4E_e E_p$ is the square of the ep c.m. energy, $\sqrt{s} = 300$ GeV. The scaling variables used to describe DIS diffraction are given by $x_{\mathcal{P}} = [(P - N) \cdot q]/(P \cdot q) \approx (M_X^2 + Q^2)/(W^2 + Q^2)$ and $\beta = Q^2/[2(P - N) \cdot q] = x/x_{\mathcal{P}} \approx Q^2/(M_X^2 + Q^2)$ where N is the four-momentum of the outgoing nucleonic system and M_X is the mass of the system into which the virtual photon dissociated. In models where diffraction is described by the t -channel exchange of a system, for example the pomeron, $x_{\mathcal{P}}$ is the momentum fraction of the proton carried by this system and β is the momentum fraction of the struck quark within this system.

3 Experimental conditions

The experimental conditions in 1994 for HERA and the ZEUS detector were described in our previous paper dealing with the F_2 measurement [19]. HERA operated with 153 colliding bunches of 27.5 GeV positrons and 820 GeV protons. Additional unpaired positron (15) and proton (17) bunches circulated, which were used to determine beam related background. The data of this analysis corresponds to a luminosity of $2.61 \pm 0.04 \text{ pb}^{-1}$.

The ZEUS apparatus is described in detail elsewhere [20]. Of particular importance for this analysis were the uranium-scintillator calorimeter (CAL) [21], the central tracking detector (CTD) [22], the small angle rear tracking detector (SRTD) [23], the proton remnant tagger (PRT) [24] and the luminosity monitor (LUMI) [25].

The CAL provides an angular coverage of 99.7% of 4π and is divided into three parts (FCAL, BCAL, RCAL), covering the forward (proton direction), central and rear regions with pseudorapidity ranges of $4.3 \leq \eta < 1.1$, $1.1 \leq \eta < -0.75$ and $-0.75 \leq \eta < -3.8$, respectively¹. Each part consists of towers which are longitudinally subdivided into electromagnetic (EMC) and hadronic (HAC) readout cells. In test beam measurements, energy resolutions of $\sigma_E/E = 0.18/\sqrt{E}$ for electrons and $\sigma_E = 0.35/\sqrt{E}$ for hadrons were obtained (E in GeV).

The CTD is a cylindrical drift chamber situated inside a superconducting solenoid which provides a 1.43 T field. It consists of 72 cylindrical layers covering the polar regions $15^\circ < \theta < 164^\circ$ and the radial range 18.2 - 79.4 cm. The transverse momentum resolution for tracks traversing all CTD layers is $\sigma(p_t)/p_t \approx \sqrt{(0.005p_t)^2 + (0.016)^2}$, with p_t in GeV. The vertex position of a typical multiparticle event is determined from the tracks to an accuracy of typically ± 1 mm in the X, Y plane and ± 4 mm in Z .

The PRT is used to tag diffractive events where the proton dissociated. The PRT consists of two layers of scintillation counters installed perpendicular to the beam at $Z = 5.15$ m,

¹The ZEUS coordinates form a right-handed system with positive- Z in the proton beam direction and a horizontal X -axis pointing towards the centre of HERA. The nominal interaction point is at $X = Y = Z = 0$. The pseudorapidity η is defined as $-\ln(\tan \frac{\theta}{2})$, where the polar angle θ is taken with respect to the proton beam direction from the nominal point.

i.e. downstream of FCAL and beam collimator C4. The two layers are separated by a 2 mm thick lead absorber. Each layer is split into two halves with two counters each which are independently read out by photomultipliers. The counters have an active area of dimensions $30 \times 26 \text{ cm}^2$ with a hole of $6.0 \times 4.5 \text{ cm}^2$ at the centre to accommodate the HERA beam pipe. The pseudorapidity covered by the PRT is $4 \lesssim \eta \lesssim 6$. The data with useful PRT information correspond to an integrated luminosity of 0.7 pb^{-1} .

4 Reconstruction of kinematic variables

The kinematic variables x, Q^2, W and M_X were determined from calorimeter and tracking information. The calorimeter cells were required to have energy deposits above 60 MeV in the EMC section and 110 MeV in the HAC section unless these energy deposits were isolated in which case thresholds of 120 MeV (160 MeV) in the EMC (HAC) sections were used. An energy-momentum vector $(E_j, p_{Xj}, p_{Yj}, p_{Zj})$ with $E_j^2 = p_{Xj}^2 + p_{Yj}^2 + p_{Zj}^2$ was assigned to every calorimeter cell j with energy deposition E_j . The cell angles were calculated from the geometric centre of the cell and the vertex position of the event. The algorithm used to identify the scattered positron was based on a neural network [26] which included information from the CAL. The systematic uncertainty in the energy determination of the scattered positron is 2% at 10 GeV decreasing linearly to 1% at 27.5 GeV for the Q^2 region considered in this analysis. The momenta of the particles of the system X were reconstructed from clusters found in the calorimeter and from tracks in the CTD [15, 27]. The inclusion of tracking information improves the M_X resolution and reduces the sensitivity to the losses due to inactive material in front of the calorimeter. A systematic uncertainty of 3% is assigned to the hadronic energy measurement. The selected clusters and tracks are called energy flow objects (EFO's).

The kinematic variables x, Q^2 and W were determined with the double angle (DA) method [28] in which only the angles of the scattered positron (θ'_e) and the produced hadronic system (γ_H) are used. The angles were determined from the EFO's. In the DA method, in order that γ_H be well measured, it is necessary to require a minimum of hadronic activity in the calorimeter away from the forward direction. A suitable quantity for this purpose is the hadronic estimator of the variable y [29], defined by $y_{JB} = \sum_j (E_j - p_{Zj}) / 2E_e$, where the sum runs over all EFO's not assigned to the scattered positron.

We study events of the type $ep \rightarrow e + X + rest$, where X denotes the hadronic system observed in the central detector (CAL and CTD) and $rest$ the particle system escaping detection through the beam holes. The mass M_X of the system X was determined by summing over all EFO's not assigned to the scattered positron:

$$(M_X^{meas})^2 = \left(\sum_j E_j\right)^2 - \left(\sum_j p_{Xj}\right)^2 - \left(\sum_j p_{Yj}\right)^2 - \left(\sum_j p_{Zj}\right)^2 \quad . \quad (2)$$

5 Trigger and event selection

The event selection at the trigger level was identical to that used for the F_2 analysis of the same data [19]. The off-line cuts were also similar to those applied previously. The energy of the scattered positron had to satisfy $E'_e > 10 \text{ GeV}$ to ensure reliable positron finding and to suppress the photoproduction background. The variable y , calculated from the scattered positron, was

required to satisfy $y_e < 0.95$ to suppress events with spurious low energy positrons. The impact point of the positron on the face of the RCAL had to lie outside a square of side 26 cm centered on the beam axis (boxcut) to ensure full containment of the positron shower. The requirement $y_{JB} > 0.02$ ensured a good measurement of the angle γ_H and hence of x . By requiring $40 < \delta < 70$ GeV, where $\delta = \sum_j (E_j - p_{Zj})$ summed over all EFO's, including those belonging to the scattered positron, both the background from photoproduction and the radiative corrections were reduced. The primary event vertex was determined from the tracks. If no tracking information was present (9.2% of the events) the vertex position was set to the nominal interaction point.

After the selection cuts and removal of events from QED Compton scattering and cosmic rays, the DIS sample contained 304k events. For the present analysis, 157k events with $60 < W < 200$ GeV, $7 < Q^2 < 140$ GeV² were used.

6 Monte Carlo simulation

Monte Carlo simulations were used for testing the validity of the subtraction of the nondiffractive contribution, for understanding the contribution from double dissociation ($\gamma^*p \rightarrow XN$), for unfolding the produced event distributions from the measured ones, for determining the acceptance and for estimating the systematic uncertainties. The detector simulation is based on the GEANT program [30] and incorporates our present understanding of the detector and the trigger and test beam results.

Hadronic final states from diffractive DIS interactions where the proton does not dissociate, $ep \rightarrow eXp$, were modelled with RAPGAP [31, 27] modified to include low-mass vector meson production. RAPGAP is based on a factorizable model [6] in which the incoming proton emits a pomeron. The interaction of the virtual photon with this pomeron is described by an effective structure function $F_2^{IP}(\beta, Q^2)$ that is independent of the process of emission of the pomeron and where the partons of the pomeron take part in the hard scattering. The parton densities of the pomeron are evolved from a starting scale $Q_0^2 = 4$ GeV² using the next-to-leading order DGLAP equations [32]. The free parameters are adjusted to reproduce the results on the diffractive structure function $F_2^{D(3)}$ measured by H1 [14]. The momentum sum rule was not imposed. RAPGAP was used with the parton showering scheme of ARIADNE 4.08 [33], which is based on the color dipole model and includes the first order QCD matrix elements, and the Lund fragmentation scheme [34] as implemented in JETSET 7.4 [35]. The region of low masses (below 1.1 GeV) is tuned to the measured ratio of $\rho : \phi$ resonance production [36, 37, 38] and allowing for a contribution from ω production.

The contribution from the diffractive process where the proton dissociates, $\gamma^*p \rightarrow XN^{dissoc}$, was simulated using EPSOFT [39]. Assuming factorisation and a Triple Regge formalism [40, 3] for modelling $\gamma^*p \rightarrow Xp$ and $\gamma^*p \rightarrow XN^{dissoc}$, the measured cross sections for elastic and single diffractive dissociation in pp (and $\bar{p}p$) scattering, $pp \rightarrow pp$ and $pp \rightarrow pN^{dissoc}$, were used to relate $\gamma^*p \rightarrow XN^{dissoc}$ to $\gamma^*p \rightarrow Xp$.

For testing the procedure used to separate the diffractive and nondiffractive contributions, events from standard nondiffractive DIS processes were produced within the framework provided by DJANGO 6.0 [41]. First order electroweak corrections were generated with HERACLES 4.5 [42]. The positron-proton kinematics was produced with LEPTO 6.5 [43] which was

interfaced to ARIADNE 4.08 for the simulation of the parton shower process. For fragmentation JETSET 7.4 was used. The parton densities of the proton were chosen to be the MRSA set [44].

All Monte Carlo events were passed through the standard ZEUS detector and trigger simulations as well as the event reconstruction package.

7 Precision of kinematic variables and binning

The resolutions expected for the kinematical variables were estimated from Monte Carlo (MC) simulation. The intervals in W were chosen with equidistant bins in $\ln W^2$, thereby providing approximately equal numbers of events in each W bin. Here, and in the following, masses and energies are given in units of GeV. The average r.m.s. resolution $\sigma(\ln W^2)$ is 0.23 in the lowest (W, Q^2) bin decreasing to 0.09 in the highest (W, Q^2) bin. A bin width of $\Delta \ln W^2 = 0.4$ was chosen. For Q^2 the r.m.s. resolution is less than 1 GeV² in the lowest Q^2 bin increasing to 3 GeV² in the highest Q^2 interval.

The mass M_X^{meas} , determined from the EFO's, has to be corrected for energy losses in the material in front of the calorimeter and for acceptance. The correction was determined by comparing, for Monte Carlo (MC) generated events, the MC measured mass, M_X^{MCmeas} , to the generated mass, M_X^{MCgen} , of the system X . The resulting corrections to determine the diffractive cross section were performed in three steps.

In the first step an overall mass correction factor was calculated from the ratios of measured to generated masses, $f(M_X^{MCmeas}) = M_X^{MCmeas}/M_X^{MCgen}$, as a function of M_X , W and Q^2 . The variation of $f(M_X^{MCmeas})$ with M_X, W, Q^2 was found to be sufficiently small ($\leq 6\%$) for the M_X range used in this analysis, $1.5 < M_X < 15$ GeV, so that it could be neglected in the first step of the mass correction. The average correction factor was $\bar{f} = 0.80$. The same correction factor was used for masses below 1.5 GeV. The correction factor \bar{f} was applied to obtain the corrected mass value, $M_X^{cor} = M_X^{meas}/\bar{f}$. The r.m.s resolution for M_X was $\sigma(M_X)/\sqrt{M_X} \approx 60\% \text{GeV}^{\frac{1}{2}}$ on average. All M_X distributions presented below refer to M_X^{cor} .

For diffractive production, a comparison of the MC-generated distributions with the MC-measured distributions show a depletion of events at the high mass end and an excess at somewhat lower mass values. This (small) distortion $r \equiv N^{MCmeas}/N^{MCgen}$ is caused mainly by particles lost through the forward beam hole. Since r was found to be independent of Q^2 , within errors, it was determined in bins of $\ln M_X^2$ for the different W intervals averaged over Q^2 yielding $\bar{r}(\ln M_X^2, W)$; no smoothing was applied to \bar{r} . The distortion was taken into account in extracting the diffractive contribution.

In the final step, the diffractive cross section was determined by an unfolding procedure discussed below taking into account, for each (M_X, W, Q^2) interval, the proper mass correction as determined from the MC simulation.

Results are presented for the intervals in W : 60 - 74, 74 - 90, 90 - 110, 110 - 134, 134 - 164, 164 - 200 GeV; in Q^2 : 7 - 10, 10 - 20, 20 - 40, 40 - 140 GeV², with average Q^2 values of 8, 14, 27, 60 GeV²; in M_X : < 3 , 3 - 7.5, 7.5 - 15 GeV, with average M_X values of 2, 5 and 11 GeV.

8 Characteristics of the M_X distributions

The method used to separate the diffractive and nondiffractive contributions is based on their very different M_X distributions. The mass distributions for typical (W, Q^2) intervals are presented in Fig. 1(top) in terms of M_X . The distributions shown were not corrected for acceptance. Two distinct groups of events are observed, one peaking at low M_X values, the other at high M_X values. While the position of the low mass peak is independent of W , the high mass peak moves to higher values as W increases.

Most of the events in the low mass peak exhibit the large rapidity gap that is characteristic of diffractive production. This may be seen from the shaded areas in Fig. 1 which show the distributions of events with $\eta_{max} < 1.5$ where η_{max} is the largest pseudorapidity at which energy deposition in the calorimeter or a track was observed. This value corresponds to a pseudorapidity gap in the detector larger than $\simeq 2.5$ units since the beam hole of the FCAL is at $\eta_{edge} \simeq 4$.

In Fig. 1(bottom) the mass distributions are presented in terms of $\ln M_X^2$. In this representation, the M_X distributions exhibit a simple scaling behaviour. The low mass peak shows up as a plateau-like structure at low $\ln M_X^2$, most notably at high W values. The shaded histograms show again the distributions of the events with a large rapidity gap, $\eta_{max} < 1.5$, which account for most of the observed plateau ². The high mass peak has a steep exponential fall-off, $d\mathcal{N}/d\ln M_X^2 \propto \exp(b \ln M_X^2)$, towards smaller $\ln M_X^2$ values. The peak position of the high mass events changes proportionally to $\ln W^2$, i.e. shows scaling in $\ln(M_X^2/W^2)$ and the slope, b , of the exponential in $\ln M_X^2$ is approximately independent of W and Q^2 . These characteristics are properties of events with uniform, random and uncorrelated particle production along the rapidity axis where particles are accepted in a limited range of rapidity. In models such as the Feynman gas model or one dominated by longitudinal phase space [46], the slope b represents the particle multiplicity per unit of rapidity. ³ The exponential in $\ln M_X^2$ and the scaling in $\ln(M_X^2/W^2)$ are directly connected to the exponential suppression of large rapidity gaps by QCD radiation. The latter populates the region between the struck quark and the coloured proton remnant.

These characteristics are also properties of realistic models for particle production in deep inelastic scattering. ARIADNE, which gives a good description of particle production by DIS at HERA, also exhibits a pure exponential fall-off with $\ln M_X^2$ and scaling in $\ln M_X^2/W^2$. This is shown in Fig. 2(top) which presents the MC simulation of the nondiffractive contribution at the generator level as a function of $\ln(M_X^2)$ for different (W, Q^2) intervals (solid histograms) where only particles generated with $\eta < 4.3$ were included. The slope b is independent of W and Q^2 , which is in agreement with the experimental observation that, for DIS events, the average charged particle multiplicity per unit of pseudorapidity η is independent of W and Q^2 [47, 48].

The comparison of the distributions at the generator level (dotted histograms) and the detector level (dashed histograms) in Fig. 2(top) shows that the exponential fall-off with $\ln M_X^2$ is not affected by detector effects.

²Note that a cut on η_{max} will select events produced by colourless exchange, from both diffraction and from reggeon exchange but does not, in general, allow the extraction of the full diffractive contribution (see also [45]).

³The pseudorapidity gap $\Delta\eta$ is related to $\ln M_X^2$ via $\Delta\eta \approx \ln(W^2/M_X^2)$ as discussed in detail in [13].

9 Extraction of the diffractive contribution

In diffractive events, the system X resulting from the dissociation of the virtual photon is almost fully contained in the detector while the outgoing proton or low mass nucleonic system escapes through the forward beam hole. Furthermore, diffractive dissociation prefers small M_X values and leads to an event distribution of the form $d\mathcal{N}/dM_X^2 \propto 1/(M_X^2)^{(1+n)}$ corresponding to $d\mathcal{N}/d \ln M_X^2 \propto 1/(M_X^2)^n$, approximately independent of W . At high energies and for large M_X , one expects $n \approx 0$, leading to a constant distribution in $\ln M_X^2$. Such a mass dependence is seen in diffractive dissociation of pp and $p\bar{p}$ scattering [1, 49]. A value of $n \approx 0$ is also expected in some models [50] - [52] for diffractive DIS as a limiting value for the fall-off of the mass distribution.

We identify the diffractive contribution as the excess of events at small M_X above the exponential fall of the nondiffractive contribution in $\ln M_X^2$. This will be referred to as the M_X method for the determination of the diffractive component. The exponential fall permits the subtraction of the nondiffractive contribution and, therefore, the extraction of the diffractive contribution without assuming the precise M_X dependence of the latter. The distribution is expected to be of the form:

$$\frac{d\mathcal{N}}{d \ln M_X^2} = D + c \exp(b \ln M_X^2), \quad \text{for } \ln M_X^2 \leq \ln W^2 - \eta_0. \quad (3)$$

Here, D denotes the diffractive contribution and the second term the nondiffractive contribution. The diffractive term D is multiplied by the distortion function $\bar{r}(\ln M_X^2, W)$ discussed above. The quantity $(\ln W^2 - \eta_0)$ specifies the maximum value of $\ln M_X^2$ up to which the exponential behaviour of the nondiffractive part holds. A value of $\eta_0 = 3.0$ was found from the data [8]. We apply Eq. 3 in a limited range of $\ln M_X^2$ to determine the parameters b and c of the nondiffractive contribution. The diffractive contribution is not taken from the fit result for D but is determined by subtracting from the observed number of events the nondiffractive contribution found from the fit values of b and c .

The diffractive contribution in various models of diffraction [50, 51, 52] is expected to be a slowly varying function of $\ln M_X^2$ when $M_X^2 > Q^2$ and to approach, in the asymptotic limit, a constant $\ln M_X^2$ distribution at large M_X , $D = \text{constant}$. The nondiffractive contribution in the (M_X, W, Q^2) bins, was determined in two steps. This procedure will be referred to as the nominal analysis. In the first step, the slope b was determined as an average over the fits to the data of the high W intervals 134 – 164, 164 – 200 GeV for $Q^2 = 7 - 10$ and 10 – 20 GeV² in the restricted M_X range, $\ln 10Q^2 < \ln M_X^2 < \ln W^2 - \eta_0$. The fits yielded $b = b_{nom} = 1.72 \pm 0.07$. This value is smaller than that predicted with ARIADNE by about 10% (see below).

In the second step, the fits were repeated for all (W, Q^2) intervals in the wide M_X range, $\ln Q^2 < \ln M_X^2 < \ln W^2 - \eta_0$, using $b = b_{nom}$ as fixed parameter and assuming $D = \text{constant}$. The fit results for the nondiffractive contribution are shown in Fig. 1 by the straight lines, those for the sum of the diffractive and nondiffractive distributions by the upper curves; the latter fluctuate since no smoothing was applied for the distortion correction \bar{r} . The fit results for the sum of the diffractive and nondiffractive contributions give a good description of the measured event distributions. Subtraction of the nondiffractive contribution yielded the number of diffractive events. From these, the diffractive cross section was obtained by unfolding. Fits were also performed with different forms for D . These were used for estimating the corresponding systematic uncertainties (see below).

The fit procedure for separating the diffractive from the nondiffractive contribution was tested with MC simulated event samples from diffractive (using RAPGAP) and nondiffractive scattering (using ARIADNE). It was first checked that the slope of the exponential fall-off for the nondiffractive contribution is not affected by detector effects. The $\ln M_X^2$ distributions predicted for the nondiffractive contribution are shown in Fig. 2(top) at the generator (dashed histograms) and detector (solid histograms) levels for the W intervals and Q^2 values. The straight lines show the fits to the MC measured distributions. The value of the slope b^{MCgen} at the generator level (average value $b^{MCgen} = 1.97 \pm 0.03$) agrees well with the value b^{MCmeas} at the detector level (average value $b^{MCmeas} = 1.96 \pm 0.03$) for each (W, Q^2) interval. Fits performed to the sum of the diffractive and nondiffractive contributions in the restricted M_X range are shown in Fig. 2(bottom). They resulted in an average slope, $b_{nom}^{MC} = 2.04 \pm 0.09$, which agrees well with the b -values found from the fits to the nondiffractive sample alone. In this figure the distributions of $\ln M_X^2$ are displayed for the sum of the diffractive and nondiffractive contributions as predicted at the detector level (points with error bars) and for the nondiffractive contribution alone (dashed histograms). In the next step, the sum of the diffractive and nondiffractive contributions were fitted in the wide M_X range using $b = b_{nom}^{MC}$. The straight lines show the nondiffractive contribution as obtained from the fits; they give a good description of the input distributions for the nondiffractive contribution shown as the dashed histograms. The upper curves show the fit results for the sum of the diffractive and nondiffractive contributions. A good description of the input distributions is observed. Using the fits with $b = b_{nom}^{MC}$, the nondiffractive contribution was subtracted which yielded, for every (W, Q^2) interval, the number of MC measured diffractive events. From this result, the number of MC produced events was determined by unfolding. Comparison with the generated (i.e. input) numbers of diffractive events showed very good agreement for all (M_X, W, Q^2) intervals.

Before applying the fitting and unfolding procedure, the number of events observed in the (M_X, W, Q^2) intervals were corrected for the contribution from positron (proton) beam gas scattering. Averaged over all events, the contamination from positron (proton)-gas scattering amounted to 2.1% (1.0%). For the nominal analysis, which did not require an event vertex, beam-gas contributions were small for $M_X > 3$ GeV and negligible for Q^2 above 20 GeV². Sizeable contributions were observed for $M_X < 3$ GeV when $W > 90$ GeV and $Q^2 < 20$ GeV² where they amounted to 14% on average for positron-gas scattering and $\leq 10\%$ for proton-gas scattering. To estimate the systematic uncertainties the analysis was also performed requiring an event vertex (see below). In this case the background from beam-gas scattering was negligible everywhere.

The number of diffractive events produced, $\mathcal{N}_{prod}^{diff}$, was obtained from the number of events determined from the fits, $\mathcal{N}_{meas}^{diff}$, by an inverse matrix unfolding procedure which took into account detector effects such as bin-to-bin migration, trigger biases and event selection cuts. It was checked that the diffractive model (RAPGAP) describes the energy flow as a function of η for $\eta_{max} < 1.5$ for all (M_X, W, Q^2) bins [27] as well as the observed M_X distributions in the region $M_X < 3$ GeV.

9.1 Contribution from nucleon dissociation

An estimate of the contribution from diffractive dissociation of the proton, $\gamma^*p \rightarrow XN^{dissoc}$, (double dissociation) to the diffractive cross section presented below was obtained by comparing the contributions for $\gamma^*p \rightarrow Xp$ (single dissociation) with an identified proton in the leading proton spectrometer LPS [15] and for $\gamma^*p \rightarrow XN$ determined in this analysis. This led to the

fractional contribution from double dissociation $(XN - Xp)/XN = XN^{dissoc}/XN = (31 \pm 15)\%$.

The procedure for extraction of the diffractive contribution was tested at the MC level also for the case where an additional contribution from diffractive dissociation of the proton was present. The events for $\gamma^*p \rightarrow XN^{dissoc}$ were simulated using EPSOFT. In Fig. 3 the $\ln M_X^2$ distributions are presented at the detector level for the diffractive contributions from $\gamma^*p \rightarrow XN^{dissoc}$ (dotted histograms) and for the sum of $\gamma^*p \rightarrow Xp + XN^{dissoc}$ (solid histograms). Also given are the nondiffractive contributions (dashed histograms) and the sum of the diffractive and nondiffractive contributions (points with error bars). Fits to the sum of the diffractive and nondiffractive contributions in the restricted M_X range yielded for the slope a value of $b^{MC(pN)} = 1.92 \pm 0.08$ in good agreement with the value $b^{MCmeas} = 1.96 \pm 0.03$ obtained before from a fit to the nondiffractive sample alone. The solid straight lines show the nondiffractive contribution as obtained from the fits; as before, they give a good description of the input distributions for the nondiffractive contribution shown as the dashed histograms and are in close agreement with the fits performed to the nondiffractive contributions alone (dashed straight lines). Using the fits and subtracting the nondiffractive contribution yielded for every (W, Q^2) interval the number of MC measured diffractive events; these were found to be in very good agreement with the number of events in the diffractive sample. This is a confirmation that the $\ln M_X^2$ method for extracting the diffractive contribution gives reliable results also in the presence of diffractive contributions where the proton dissociated.

Only a limited mass (M_N) range of N^{dissoc} contributes to the diffractive cross section presented below. This was studied with EPSOFT. The distribution of the generated mass M_N peaks at low values, $M_N \lesssim 2$ GeV. Due to the dominance of small M_N values the secondaries from N^{dissoc} are strongly collimated around the direction of the incoming proton. Analysis of the angular distribution of the secondaries as a function of M_N showed that for $M_N < 2$ GeV basically no energy is deposited in the calorimeter, while for events with $M_N > 6$ GeV there are almost always secondaries which deposit energy in the calorimeter. Furthermore, events of the type $\gamma^*p \rightarrow XN^{dissoc}$, where decay particles from N^{dissoc} deposit energy in the calorimeter, have in general a reconstructed mass which is substantially larger than the mass of X and, therefore, these events contribute little to the event sample selected for diffractive production of $\gamma^*p \rightarrow XN$.

As a result, for each M_X bin there is an M_N value, called M_N^{accept} , such that the number of events with $M_N < M_N^{accept}$, which migrate outside the bin is equal to those with $M_N > M_N^{accept}$, which migrate into this bin. For the (M_X, W, Q^2) bins studied M_N^{accept} was found to be 5.5 GeV to within ± 1.5 GeV. The spread in the value of M_N^{accept} introduces an uncertainty in the cross section measurements which is below the statistical uncertainty. Therefore, the diffractive cross sections are quoted below as cross sections for $\gamma^*p \rightarrow XN$ with $M_N < 5.5$ GeV.

In the nominal analysis, the unfolding of the diffractive contribution was performed considering only dissociation of the virtual photon as simulated with RAPGAP. In order to test the sensitivity of the unfolding to a contribution from double dissociation, the nominal unfolding procedure was also applied to a MC sample consisting of a mixture of single and double dissociation in the proportion given above for the measured region. The resulting cross section gave a good match to the cross section with $M_N < 5.5$ GeV as input.

An attempt was made to estimate quantitatively the contribution from proton dissociation by studying those events where a signal was recorded in the PRT. The PRT registers particles

emitted at large pseudorapidities, $\eta = 4 - 6$. Such particles may result from diffractive production where the proton dissociated or from diffractive dissociation of the virtual photon into a system with a large M_X , and from the proton remnant in nondiffractive production. The points with error bars in Fig. 4 show for the subset of the data with useful PRT information the $\ln M_X^2$ distributions for all events. The straight lines show the nondiffractive contribution as obtained from the fits performed in the wide M_X range. The sum of the diffractive and nondiffractive contributions as obtained from the fits (upper curves) are in good agreement with the data. The solid histograms in Fig. 4 show the distributions (called PRT-tagged distributions) for events with a PRT signal. Most of the events in the high $\ln M_X^2$ peak have a PRT signal as expected for nondiffractive scattering. The exponential fall-off of the PRT-tagged distributions agrees well with the predictions obtained from the fits for the nondiffractive contributions as shown by the straight lines. This gives additional experimental proof for the reliability of the M_X method.

A fraction of the events in the low mass region also has a PRT signal. MC simulation showed that for $M_X < 3$ GeV almost all events with a PRT signal are diffractive events where the proton dissociated. From the number of PRT tagged events in this region, using the efficiencies determined for the PRT counters [53] and the prediction from EPSOFT for the PRT acceptance, events from diffractive dissociation via $\gamma^*p \rightarrow XN^{dissoc}$ contribute an estimated fraction of $XN^{dissoc}/XN = 27 \pm 2(stat)\%$ (plus an unknown systematic uncertainty which depends on the mass spectrum and decay properties of N^{dissoc}) to the diffractive cross sections presented below. We prefer the estimate obtained by comparison with the LPS analysis over that obtained here with the PRT since the former does not rely on an assumption for the properties of N^{dissoc} .

10 Evaluation of the cross sections

For the final analysis, only bins where the fraction of nondiffractive background was less than 50% and the purity was above 30% were kept. Purity is defined as the ratio of the number of events generated in the bin and observed in the same bin divided by the total number of events observed in the bin. The average purity in the (M_X, W, Q^2) bins was 52 %. The nondiffractive background fraction was small for low M_X or large W values: for $M_X < 3$ GeV the background fraction was typically below 2% except for $Q^2 = 27$ (60) GeV² where in the lowest W bin for which cross sections are presented it amounted to 10% (17%). For $3 < M_X < 7.5$ GeV the background fraction was typically below 5% except for the next-to-lowest (lowest) W bin where it reached 18% (33%). For $7.5 < M_X < 15$ GeV the numbers were 22 - 37% in the lowest bin and typically 15% elsewhere.

The average differential cross section for ep scattering, in a given (M_X, W, Q^2) bin, was obtained by dividing the number of unfolded events, $\mathcal{N}_{prod}^{diff}$, by the luminosity, the bin widths and the QED radiative correction factor. The lower limit of M_X was taken to be $2m_\pi$, where m_π is the pion mass.

The cross section for the process $ep \rightarrow eXN$ can be expressed in terms of the transverse (T) and longitudinal (L) cross sections, σ_T^{diff} and σ_L^{diff} , for $\gamma^*p \rightarrow XN$ as [55]:

$$\frac{d\sigma_{\gamma^*p \rightarrow XN}^{diff}(M_X, W, Q^2)}{dM_X} \equiv \frac{d(\sigma_T^{diff} + \sigma_L^{diff})}{dM_X} \approx \frac{2\pi}{\alpha} \frac{Q^2}{(1-y)^2 + 1} \frac{d\sigma_{ep \rightarrow eXN}^{diff}(M_X, W, Q^2)}{dM_X d \ln W^2 dQ^2}. \quad (4)$$

Here, a term $[1 - \frac{y^2}{(1-y)^2+1} \frac{\sigma_L^{diff}}{\sigma_T^{diff} + \sigma_L^{diff}}]$ multiplying $[\sigma_T^{diff} + \sigma_L^{diff}]$ has been neglected. Since $y \approx W^2/s$, this term can be substantially different from unity only at high W values. The effect is less than 5% if $W < 158$ GeV corresponding to $y \approx W^2/s < 0.28$, or if $W < 200$ GeV and $\sigma_L^{diff} < 0.5\sigma_T^{diff}$. In the extreme case that $\sigma_L^{diff} \gg \sigma_T^{diff}$, the term will increase $[\sigma_T^{diff} + \sigma_L^{diff}]$ by at most 11% for the highest W bin (164 - 200 GeV).

The differential cross section $d\sigma_{\gamma^*p \rightarrow XN}^{diff}/dM_X$ was determined from Eq.(4) in the different (M_X, W, Q^2) intervals using the fit results obtained assuming a constant D and transported to convenient values of M_X and Q^2 using the shape of the parametrization of [54] (see below).

Systematic errors: The systematic uncertainties for the cross section were estimated in a similar way as in the previous work [13] by varying the cuts and algorithms used to select the events at the data and MC levels and repeating the full analysis for every variant. The uncertainties in selecting the DIS events arising from the identification of the scattered positron were estimated by varying the box cut, the minimum energy and the minimum probability required for the scattered positron. The uncertainties in the reconstruction of the hadronic system were estimated by varying the y_{JB} cut between 0.01 and 0.03. In each case the deviations from the nominal result were well below 10% and typically 1 - 3%. The uncertainty due to the beam-gas background was determined by removing events without a reconstructed event vertex. This resulted in small differences of up to 13%. In order to test for remaining background from photoproduction and the sensitivity to radiative effects the cut on $\sum_j(E_j - p_{Zj})$ was varied. This resulted in small changes except for three (M_X, W, Q^2) bins where differences of up to 14% were seen, commensurate with the corresponding statistical errors.

Variation of the noise cuts for isolated calorimeter cells had a negligible effect. Allowing for $\pm 5\%$ differences in the M_X correction between data and MC simulation to account for uncertainties in the energy scale of the calorimeter and the material in front affected mainly the low M_X bin, where at higher Q^2 values, differences of up to 11% were found. Note that increasing (lowering) the mass correction factor systematically decreases (increases) the cross section. Since the relative changes are basically independent of W this does not affect the W dependence of the cross section. The acceptance corrections and unfolding were also performed with a different model for diffraction ⁴. For $Q^2 < 27$ GeV² the differences were typically a few percent reaching values between 11% and 18% in four bins. In the highest Q^2 bin the differences were $\leq 14\%$ except for the low M_X bin where they reached up to 57%; this is mainly due to the small event numbers involved.

The nominal fitting procedure for subtracting the nondiffractive background used the fixed slope $b = b_{nom}$, see Section 9. The analysis was also performed with b determined for the high W bins 134 - 164, 164 - 200 GeV from the wide M_X range using for D the extended form: $D = d_0(1-\beta)[\beta(1-\beta) + \frac{d_1}{2}(1-\beta)^2]$, and the variable form: $D = d_0(1-\beta)[\beta(1-\beta) + \frac{d_1}{2}(1-\beta)^g]$, where d_0, d_1 and g are parameters [50] - [54]. Both forms consist of a quark-like (first term) and a gluon-like (second term) contribution. In the wide M_X range the quark-like contribution decreases with $\ln M_X^2$ while the gluon-like term increases. In the fits with the variable form the gluon-like term dominates at large masses which leads to $D = constant$ in the asymptotic limit. The resulting changes of the diffractive cross section were small and did not exceed 13%. For the extended form, typical differences of 10 - 25% were found; the largest difference was found for one bin at $Q^2 = 60$ GeV² and amounted to -37%.

⁴In this case diffraction was modelled in RAPGAP using the parametrization developed in [13] on the basis of the model of [50].

The total systematic error for each bin was determined by quadratically adding the individual systematic uncertainties, separately for the positive and negative contributions. The total errors were obtained by adding the statistical and systematic errors in quadrature. The errors do not include an overall normalization uncertainty of 2% of which 1.5% is from the luminosity determination and 1.0% from the uncertainty in the trigger efficiency.

11 Differential cross section for $\gamma^*p \rightarrow X N$

11.1 W and Q^2 dependence of $d\sigma_{\gamma^*p \rightarrow XN}^{diff}/dM_X$

The diffractive cross section for $\gamma^*p \rightarrow XN$, ($M_N < 5.5$ GeV), is presented in Table 1 and Fig. 5 as a function of W for various M_X and Q^2 values. From comparison with published data [36] - [38], about 20% of the diffractive cross section observed in the mass bin $M_X < 3$ GeV at $7 < Q^2 < 20$ GeV² results from the production of the vector mesons $V = \rho^0, \phi$ via $\gamma^*p \rightarrow VN$. In Fig. 6 $Q^2 d\sigma_{\gamma^*p \rightarrow XN}^{diff}/dM_X$ is presented as a function of Q^2 for different (M_X, W) values. A fast decrease with Q^2 is observed for small M_X which is similar to the behaviour of DIS vector meson production [36] - [38]. The decrease becomes slower for the high M_X region showing that high mass dissociation of the virtual photon becomes increasingly more important as Q^2 grows. For a discussion in terms of a partonic behaviour see below.

The diffractive cross section rises rapidly with W at all Q^2 values for the M_X bins up to 7.5 GeV. The cross section was fitted [56] for each (M_X, Q^2) bin using the form

$$\frac{d\sigma_{\gamma^*p \rightarrow XN}^{diff}(M_X, W, Q^2)}{dM_X} = h \cdot W^{a^{diff}} \quad , \quad (5)$$

where a^{diff} and the normalization constants h were treated as free parameters. The form given in Eq. 5 with a single value of a^{diff} gives an acceptable χ^2 value ($\chi^2/d.o.f. = 37/35 = 1.1$), considering only the statistical errors) although one observes in Fig. 5 (see dashed curves) a tendency for the data at low M_X , high Q^2 to have a steeper slope than resulting from this fit. The fit yielded $a^{diff} = 0.507 \pm 0.034(stat)_{-0.046}^{+0.155}(syst)$. Here, the largest contribution to the positive systematic error arises when the extended form is used for D in the determination of the slope b . In Regge models, a^{diff} is related to the trajectory of the pomeron $\alpha_P(t)$, averaged over t : $\overline{\alpha_P} = 1 + a^{diff}/4$. The fit value for a^{diff} leads to $\overline{\alpha_P} = 1.127 \pm 0.009(stat)_{-0.012}^{+0.039}(syst)$.

In order to test for a possible Q^2 dependence of $\overline{\alpha_P}$ a fit was performed where a^{diff} was taken as a free parameter for every (M_X, Q^2) bin. This resulted also in a good description of the data (see solid curves in Fig. 5). The resulting $\overline{\alpha_P}$ values are shown in Fig. 7 with the statistical and systematic uncertainties added in quadrature. The systematic uncertainties were estimated by repeating the fits independently for every source of systematic error. With the present accuracy of the data, no conclusion can be drawn on a possible Q^2 dependence of $\overline{\alpha_P}$.

In deriving the diffractive cross section, the assumption was made that the term

$[1 - \frac{y^2}{(1-y)^2+1} \frac{\sigma_L^{diff}}{\sigma_T^{diff} + \sigma_L^{diff}}]$ can be neglected (see Eq. 4). This holds when $\sigma_L^{diff} \ll \sigma_T^{diff}$. If the assumption is made that $\sigma_L^{diff} = \sigma_T^{diff}$ ($\sigma_T^{diff} \ll \sigma_L^{diff}$) the value of a^{diff} increases by 0.047 (0.096) and hence $\overline{\alpha_P}$ increases by 0.012 (0.024).

H1 [14] has given for the intercept of the pomeron trajectory a value of $\alpha_p(0) = 1.203 \pm 0.020(stat) \pm 0.013(syst)_{-0.035}^{+0.030}(model)$. Averaging over the t -distribution ⁵ gives approximately $\overline{\alpha_p} = \alpha_p(0) - 0.03$, a value which is consistent with the result from this analysis ⁶.

Our value of $\overline{\alpha_p} = 1.127 \pm 0.009(stat)_{-0.012}^{+0.039}(syst)$ lies above the results deduced from hadron-hadron scattering where the intercept of the pomeron trajectory was found to be $\alpha_p^{soft}(0) = 1.08$ [5] and $\alpha_p^{soft}(0) = 1.096_{-0.009}^{+0.012}$ [57]. Averaging over t reduces these values by about 0.02 ⁷ leading to $\overline{\alpha_p}^{soft} = 1.06$ [5] and $\overline{\alpha_p}^{soft} = 1.076_{-0.009}^{+0.012}$, respectively. The latter value is shown by the horizontal bands in Fig. 7.

11.2 Comparison of the diffractive and total cross sections

The ratio of the diffractive cross section to the total virtual-photon proton cross section,

$$r_{tot}^{diff} = \frac{\int_{M_a}^{M_b} dM_X d\sigma_{\gamma^*p \rightarrow XN}^{diff}/dM_X}{\sigma_{\gamma^*p}^{tot}}, \quad (6)$$

is displayed in Fig. 8 as a function of W for the different M_X bins ($M_a < M_X < M_b$) and Q^2 values. The total cross section was taken from our F_2 measurements performed with the 1994 data [19] using $\sigma_{\gamma^*p}^{tot}(W, Q^2) = \frac{4\pi^2\alpha}{Q^2(1-x)}F_2(x \approx \frac{Q^2}{W^2}, Q^2)$. The data show that, for fixed M_X , the diffractive cross section possesses the same W dependence as the total cross section. A fit of r_{tot}^{diff} using the form $r_{tot}^{diff} \propto W^\rho$, considering all data with $M_X < 7.5$ GeV and treating ρ and the normalization constants for every (M_X, Q^2) interval as free parameters, yielded $\rho = 0.00 \pm 0.03(stat)$, consistent with W independence. The same conclusion is reached when comparing the value of the power $a^{diff} = 0.507 \pm 0.034(stat)_{-0.046}^{+0.155}(syst)$ with the power $a^{tot} = 0.55 \pm 0.02$ obtained for $\sigma_{\gamma^*p}^{tot}$ in the same (W, Q^2) range. Equal powers for the diffractive and total cross sections is contrary to the naïve expectation. Assuming (i) for DIS the validity of the optical theorem [59] and (ii) that the cross section for diffractive photon dissociation at fixed M_X has the same W dependence as the forward cross section for elastic scattering, $\gamma^*p \rightarrow \gamma^*p$, then $d\sigma_{\gamma^*p \rightarrow XN}^{diff}/dM_X$ should be proportional to W^a if $\sigma_{\gamma^*p}^{tot} \propto W^{a/2}$. Hence, taking the W dependence found for $d\sigma_{\gamma^*p \rightarrow XN}^{diff}/dM_X$ the power ρ would have been expected to be $\rho = a^{diff}/2 = 0.25 \pm 0.02(stat)_{-0.02}^{+0.07}(syst)$, in clear disagreement with the data.

The rapid rise of σ_{tot} with W , which is equivalent to the rapid rise of F_2 as $x \rightarrow 0$, in QCD is attributed to the evolution of partonic processes. The observation of similar W dependences for the total and diffractive cross sections suggests, therefore, that diffraction in DIS receives sizeable contributions from hard processes. The same W dependence for the diffractive and total cross sections was predicted in [60] (see below).

The diffractive contribution to the total cross section for low M_X decreases rapidly as Q^2 increases while for $M_X = 11$ GeV it is the same, within a factor of two. Averaged over $W =$

⁵When parametrizing the t -distribution by $d\sigma/dt \propto \exp[(b_0 + 2\alpha_p' \ln(1/x_{IP}))t]$ the difference $\alpha_p(0) - \overline{\alpha_p}$ is determined mainly by b_0 and α_p' . H1 quotes $b_0 = 4.6 \text{ GeV}^{-2}$ and $\alpha_p' = 0.26 \text{ GeV}^{-2}$.

⁶In the analysis of H1 [14] the diffractive contribution was first extracted by selecting events with a large rapidity gap. From the x_p dependence of the resulting diffractive structure function $F_2^{D(3)}(x_p, \beta, Q^2)$ it was concluded that at large x_p a substantial reggeon contribution was present. The latter was determined from a Regge fit to the data using the sum of a pomeron and a reggeon contribution. We have performed a similar fit to our data and found no evidence for a significant contribution from reggeon exchange.

⁷Assuming for the t -distribution $d\sigma/dt \propto \exp[(b_0 + 2\alpha_p' \ln W^2)t]$ with $b_0 = 7 \text{ GeV}^{-2}$ (from π^-p elastic scattering, see [1]) and $\alpha_p' = 0.25 \text{ GeV}^{-2}$ [5].

60 – 200 GeV (considering only the accepted bins), the diffractive contribution (with $M_N < 5.5$ GeV) to the total cross section for $M_X < 7.5$ GeV is $9.2^{+0.3\%}_{-0.4\%}$ ($6.3^{+0.3\%}_{-0.3\%}$, $3.9^{+0.2\%}_{-0.3\%}$, $1.3^{+0.2\%}_{-0.2\%}$) at $Q^2 = 8(14, 27, 60)$ GeV². The corresponding fractions for $M_X < 15$ GeV in the W range 134 - 200 GeV are $13.2^{+0.5\%}_{-0.7\%}$ ($9.4^{+0.5\%}_{-0.6\%}$, $7.5^{+0.3\%}_{-0.5\%}$, $3.7^{+0.3\%}_{-0.4\%}$). As Q^2 increases, the high M_X region becomes more important.

The Q^2 behaviour of the diffractive contribution to the total cross section observed here for $M_X < 15$ GeV is not in contradiction to our earlier finding that the fraction of DIS events with a large rapidity gap (LRG) is rather constant with Q^2 [8]: the LRG analysis considered events with masses $M_X \gtrsim 4$ GeV, did not impose an upper limit on M_X and included the W range up to 270 GeV.

12 Diffractive structure function of the proton

The concept of a diffractive structure function introduced in [6] is based on the assumption that diffraction is mediated by the exchange of a colourless object, called a pomeron, which is composed of partons. The diffractive structure function of the proton can be related to the diffractive cross section as follows [16]:

$$\frac{1}{2M_X} \frac{d\sigma_{\gamma^*p \rightarrow XN}^{diff}(M_X, W, Q^2)}{dM_X} = 4\pi^2\alpha \frac{W^2}{(Q^2 + W^2)^2 Q^2} F_2^{D(3)}(\beta, x_p, Q^2). \quad (7)$$

For $W^2 \gg Q^2$, which holds for this analysis, Eq. 7 can be written as:

$$\frac{1}{2M_X} \frac{d\sigma_{\gamma^*p \rightarrow XN}^{diff}(M_X, W, Q^2)}{dM_X} \approx \frac{4\pi^2\alpha}{Q^2(Q^2 + M_X^2)} x_p F_2^{D(3)}(\beta, x_p, Q^2). \quad (8)$$

If $F_2^{D(3)}$ is interpreted in terms of quark densities then it specifies for a diffractive process the probability to find a quark carrying a momentum fraction $x = \beta x_p$ of the proton momentum.

It has been suggested [6] that $F_2^{D(3)}(x_p, \beta, Q^2)$ should factorize into a term which depends on the probability of finding a pomeron carrying a fraction x_p of the proton momentum and the pomeron structure function $F_2^{D(2)}$ given in terms of the pomeron's quark densities which depend on β and Q^2 :

$$F_2^{D(3)}(x_p, \beta, Q^2) = f_{IP}(x_p) F_2^{D(2)}(\beta, Q^2) \quad (9)$$

where $f_{IP}(x_p)$ is generically called the pomeron flux factor.

The quantity $x_p F_2^{D(3)}$ is given in Table 2 and shown in Fig. 9 as a function of x_p for different combinations of β and Q^2 .

In Fig. 10 the data from this analysis (solid points) are compared with ZEUS data obtained using the Leading Proton Spectrometer (LPS) [15] and with those of H1 [14]. For ease of comparison the $x_p F_2^{D(3)}$ values from this analysis were scaled to the (β, Q^2) values used in the H1 analysis. The LPS data correspond to events of the type $\gamma^*p \rightarrow Xp$ with an identified proton. No correction was applied for the contribution from double dissociation which is present in this analysis but not in the LPS data. The correction would increase the LPS data by a factor of $1.45^{+0.34}_{-0.23}$. There is consistency between this analysis and the LPS data. The H1 data correspond to $M_N < 1.6$ GeV while those from this analysis are given for $M_N < 5.5$ GeV. No correction was applied. The data from H1 approximately agree with those from this analysis. However, for fixed β , the H1 values have a tendency to rise faster with Q^2 even allowing for an extra scaling factor.

12.1 x_P dependence of $x_P F_2^{D(3)}(x_P, \beta, Q^2)$

The data from this analysis (Fig. 9) show that $x_P F_2^{D(3)}(x_P, \beta, Q^2)$ decreases with increasing x_P , which reflects the rapid increase of the diffractive cross section with rising W . Assuming the flux factor to be of the form $f_{\mathcal{P}}(x_P) = (C/x_P) \cdot (x_0/x_P)^n$, taking for the arbitrary normalization constant $C = 1$ and for x_0 the average value of the measured x_P , $x_0 = 0.0042$, the data were fitted with the form $x_P F_2^{D(3)}(x_P, \beta, Q^2) = (C/x_P) \cdot (x_0/x_P)^n F_2^{D(2)}(\beta, Q^2)$, which leads to $F_2^{D(2)}(\beta, Q^2) = x_0 F_2^{D(3)}(x_0, \beta, Q^2)$. The values $F_2^{D(2)}(\beta_i, Q_i^2)$ at the 12 measured (β_i, Q_i^2) points and n were treated as fit parameters. A good fit was obtained ($\chi^2/d.o.f. = 41/40 = 1.0$, statistical errors only) yielding $n = 0.253 \pm 0.017(stat)_{-0.023}^{+0.077}(syst)$. Note that $n \simeq a^{diff}/2 = 2(\overline{\alpha_P} - 1)$. The fit was also performed assuming n to depend logarithmically on Q^2 . This resulted in small differences that were included in the errors given for $F_2^{D(2)}$. The fact that a good fit was found with a single value for n shows that the data are consistent with the assumption that $F_2^{D(3)}$ factorizes into a flux factor depending only on x_P and a structure function $F_2^{D(2)}$ which depends on (β, Q^2) . Note that there is an arbitrary normalization factor for the flux and therefore also for $F_2^{D(2)}$.

12.2 β and Q^2 dependence of $x_P F_2^{D(3)}(x_P, \beta, Q^2)$ and $F_2^{D(2)}(\beta, Q^2)$

The $F_2^{D(2)}(\beta, Q^2)$ values obtained from the fit described above are presented in Fig. 11 as a function of β for all Q^2 values. It should be stressed that these $F_2^{D(2)}$ values do not depend on whether the $F_2^{D(3)}$ factorizes into a pomeron flux factor or not since a) $F_2^{D(2)}(\beta, Q^2) = x_0 F_2^{D(3)}(x_0, \beta, Q^2)$ and the fit was basically only used to interpolate to $x_P = x_0$; b) a fit with a Q^2 dependent flux gave basically the same $F_2^{D(2)}$ values. The data show that the diffractive structure function $F_2^{D(2)}$ has a simple behaviour. For $\beta < 0.6$ and $Q^2 < 14 \text{ GeV}^2$, $F_2^{D(2)}$ is approximately independent of β . For $\beta < 0.8$ also the data from different Q^2 values are rather similar suggesting a leading twist behaviour characterized by a slow $\ln Q^2$ type rescaling. For $\beta > 0.9$ the data show a decrease with β or Q^2 .

The Q^2 behaviour of $x_P F_2^{D(3)}(x_P, \beta, Q^2)$ is shown as solid points in Fig. 12. The data are presented for fixed (M_X, W) , the variables in which the diffractive contribution was extracted. Given (M_X, W) and Q^2 the value of x_P can be calculated. For $M_X < 7.5 \text{ GeV}$, $x_P F_2^{D(3)}$ decreases with Q^2 while for $M_X = 11 \text{ GeV}$ it is approximately constant.

Strong Q^2 variations, which are found e.g. for the diffractive cross section (see Fig. 6), are just a reflection of kinematics: the strong Q^2 variation of $Q^2 d\sigma_{\gamma^*p \rightarrow XN}^{diff}/dM_X$ is mainly controlled by the kinematical factor $M_X/(Q^2 + M_X^2)$ in Eq. 8.

The approximate constancy of $F_2^{D(2)}$ for $\beta < 0.9$ combined with the rapid rise of $F_2^{D(3)}$ as x_P decreases can be interpreted as evidence for a substantial partonic component in DIS diffractive dissociation.

12.3 Comparison with models

The diffractive process in DIS has attracted considerable attention because of the possibility that this process can be described by perturbative QCD (pQCD). In parton models the process

can be visualized as a fluctuation of the incoming virtual photon into a $q\bar{q}$ pair followed by the interaction of this pair with the incoming proton leading to a $q\bar{q}$ state plus, well separated in rapidity, a proton or debris from the dissociation of the proton. In [62] it was argued that the dominant contribution to diffraction in DIS comes from the aligned jet configuration where q and \bar{q} from photon dissociation have small transverse momenta relative to the direction of the virtual photon leading to the same energy dependence as observed for diffraction in hadron-hadron scattering. This contribution was expected to scale with Q^2 . The β distribution for the aligned jet configuration from transverse photons was predicted [63] to be of the form

$$F_{q\bar{q}}^T \propto \beta(1 - \beta). \quad (10)$$

The same β dependence was expected in pQCD when the aligned quarks interact with the proton through two-gluon exchange [50]. The production of a $q\bar{q}g$ system by transverse photons was also found to be leading twist and was assumed to have a β dependence of the type [50]

$$F_{q\bar{q}g}^T \propto (1 - \beta)^\gamma \quad (11)$$

with $\gamma = 2$. A later calculation [64] found $\gamma = 3$. In the same approach the contribution to the production of a $q\bar{q}$ system by longitudinal photons was found to be of higher twist and to have a β dependence of the form

$$F_{q\bar{q}}^L \propto \beta^3(1 - 2\beta)^2. \quad (12)$$

In pQCD models the x_p dependence is expected to be driven by the x dependence of the square of the gluon momentum density of the proton [68], $[x \cdot g(x, \mu^2)]^2$, with $x = x_p$ and μ is the probing scale.

In [65] the sum of the contributions from the three terms $F_{q\bar{q}}^T, F_{q\bar{q}}^L, F_{q\bar{q}g}^T$ was evaluated in the perturbative region.

We now compare the data with three partonic models (NZ) [50], (BPR) [67] and (BEKW) [54]. In the NZ model, diffractive dissociation is described as a fluctuation of the photon into a $q\bar{q}$ or $q\bar{q}g$ Fock state [50]. The interaction with the proton proceeds via the exchange of a BFKL [66] type pomeron, starting in lowest order from the exchange of a two-gluon system in a colour-singlet state. The BPR model describes the process $\gamma^*p \rightarrow Xp$ as the scattering of a colour dipole from the photon on a colour dipole from the proton. The model parameters were chosen by comparison with the H1 data [14]. The predictions of the NZ and BPR models are shown in Fig. 9 for $x_p F_2^{D(3)}$ as a function of x_p by the dashed and dotted curves, respectively. The NZ model provides a reasonable description of the data. The BPR model has some difficulties in reproducing the data for medium values of β and $Q^2 < 14 \text{ GeV}^2$.

We studied the individual contributions from the three terms in Eqs. 10- 12 following [54] which identified them as the major contributors to the diffractive structure function. In [54] they were calculated in the perturbative region and extended into the soft region. The x_p dependence was assumed to be of the form $(1/x_p)^n$. The power n was allowed to be different for the transverse (n_T) and the longitudinal (n_L) contributions. The normalizations of the three terms were determined from the data. This is called the BEKW model in the following:

$$x_p F_2^{D(3)}(\beta, x_p, Q^2) = c_T \cdot F_{q\bar{q}}^T + c_L \cdot F_{q\bar{q}}^L + c_g \cdot F_{q\bar{q}g}^T \quad (13)$$

with

$$F_{q\bar{q}}^T = \left(\frac{x_0}{x_P}\right)^{n_T(Q^2)} \cdot \beta(1 - \beta) \quad (14)$$

$$F_{q\bar{q}}^L = \left(\frac{x_0}{x_P}\right)^{n_L(Q^2)} \cdot \frac{Q_0^2}{Q^2} \cdot \left[\ln\left(\frac{7}{4} + \frac{Q^2}{4\beta Q_0^2}\right)\right]^2 \cdot \beta^3(1 - 2\beta)^2 \quad (15)$$

$$F_{q\bar{q}g}^T = \left(\frac{x_0}{x_P}\right)^{n_T(Q^2)} \cdot \ln\left(1 + \frac{Q^2}{Q_0^2}\right) \cdot (1 - \beta)^\gamma \quad (16)$$

$$n_{T,L}(Q^2) = 0.1 + n_{T,L}^0 \cdot \ln\left[1 + \ln\left(\frac{Q^2}{Q_0^2}\right)\right]. \quad (17)$$

The three terms behave differently as a function of Q^2 . Except for a possible Q^2 dependence of the power n_T , $F_{q\bar{q}}^T$ does not depend on Q^2 as a result of the limited quark p_T in the aligned configuration. The term $F_{q\bar{q}}^L$ is higher twist but the power $1/Q^2$ is softened by a logarithmic Q^2 factor; $F_{q\bar{q}g}^T$ grows logarithmically with Q^2 similar to the proton structure function F_2 at low x .

The coefficients c_T, c_L, c_g as well as the parameters n_T^0, n_L^0 and x_0, Q_0^2 were determined from experiment. In the fit the power γ was also considered as a free parameter. Assuming $Q_0^2 = 1 \text{ GeV}^2$ and $x_0 = 0.0042$ and treating the other constants as free parameters a good fit ($\chi^2/d.o.f. = 56/47 = 1.2$, statistical errors only) was obtained for the $x_P F_2^{D(3)}(x_P, \beta, Q^2)$ data from this analysis as shown by the solid curves in Fig. 9. The fit yielded the following parameter values: $n_T^0 = 0.13 \pm 0.03$, $n_L^0 = 0.32 \pm 0.14$, $\gamma = 3.9 \pm 0.9$, $c_T = 0.11 \pm 0.01$, $c_L = 0.12 \pm 0.03$, $c_g = 0.014 \pm 0.002$; the errors include the statistical and systematic uncertainties combined in quadrature.

The BEKW model also describes the Q^2 dependence of $x_P F_2^{D(3)}$ as shown by the solid curves in Fig. 13, and the β (and Q^2) dependence of $F_2^{D(2)}$ shown in Fig. 11. The value $\gamma = 3.9 \pm 0.9$ is consistent with the prediction of [64], $\gamma = 3$, and somewhat higher than the value $\gamma = 2$ given in [50].

It is instructive to compare the β and Q^2 dependences of the three components which build up the diffractive structure function $F_2^{D(3)}$ in the BEKW model using the results from the fit. Figure 14(top) shows $c_T F_{q\bar{q}}^T$ (dashed), $c_L F_{q\bar{q}}^L$ (dashed-dotted), $c_g F_{q\bar{q}g}^T$ (dotted) and their sum $x_P F_2^{D(3)}(x_P, \beta, Q^2)$ at $x_P = x_0$ (solid curves) as a function of β for $Q^2 = 8, 14, 27, 60 \text{ GeV}^2$. Our data suggest that for $\beta > 0.2$ the colourless system couples predominantly to the quarks in the virtual photon. The region $\beta \geq 0.8$ is dominated by the contributions from longitudinal photons⁸. The contribution from coupling of the colourless system to a $q\bar{q}g$ final state becomes important for $\beta < 0.3$. The last result is in contrast to the H1 observation [14] that, using a DGLAP NLO fit, the large β region is dominated by the gluon contribution⁹.

Figure 14(bottom) shows the same quantities as a function of Q^2 for $\beta = 0.1, 0.5, 0.9$. The gluon term, which dominates at $\beta = 0.1$ rises with Q^2 while the quark term, which is important at $\beta = 0.5$ shows no evolution with Q^2 . The contribution from longitudinal photons, which is higher twist and dominates at $\beta = 0.9$, decreases with Q^2 .

⁸In determining the diffractive cross section and the diffractive structure function the term $\left[1 - \frac{y^2}{(1-y)^2+1} \frac{\sigma_L^{diff}}{\sigma_L^{diff} + \sigma_T^{diff}}\right]$ has been neglected, see Eq. 4. If this term is kept for $\beta > 0.8$ and the BEKW fit is repeated with the assumption $\sigma_L = \sigma_T$ the changes in the fit parameters are small compared to their errors.

⁹In [54] two possible solutions were found from fits to the H1 data: one where the gluon term is dominant at large β and one where it is not. The latter had a slightly larger χ^2 value.

In the BEKW model the x_p -dependence of the quark and gluon contributions for transverse photons is expected to be close to that given by the soft pomeron, $n_T \approx 2(\overline{\alpha}_P^{soft} - 1)$. However, perturbative admixtures in the diffractive final state are expected to have a somewhat stronger energy dependence, leading to an effective $n_T > 2(\overline{\alpha}_P^{soft} - 1)$. The x_p dependence of the longitudinal contribution is driven by the square of the proton's gluon momentum density leading to $n_L > n_T$. The fit results agree with these predictions but the errors are too large for a definitive statement.

The same conclusion is reached when separate fits are performed for the regions $\beta \geq 0.8$ and $\beta < 0.8$. Assuming $n = n_T = n_L$ the results are $n(\beta \geq 0.8) = 0.46 \pm 0.12$ and $n(\beta < 0.8) = 0.27 \pm 0.03$. It is important to note that already at $Q^2 = 8 \text{ GeV}^2$, $n_T(Q^2 = 8 \text{ GeV}^2) = 0.25 \pm 0.04$ which is substantially larger than the expectation for soft contributions, $n_{soft} = 0.152_{-0.018}^{+0.024}$, indicating that the transverse and gluon components receive sizeable contributions from perturbative processes.

In the BH model [60] the x_p and Q^2 dependences of the diffractive structure function at small x_p have been related to the x and Q^2 dependences of the structure function F_2 by assuming that in diffractive DIS a colourless cluster σ is separated from the proton which interacts with the virtual photon. The probability, $\sigma(x_p, Q^2)$, for finding such a cluster in the proton at small x_p is expected to have an x_p dependence similar to the x dependence of the quark and gluon densities in the proton, $g(x, Q^2)$, $q_{sea}(x, Q^2)$, provided $x = x_p$. Since diffractive DIS is expected to predominantly produce configurations where the relative transverse momenta of at least one pair of partons are small, QCD evolution is suppressed in contrast to inclusive deep-inelastic scattering. These arguments have led to the prediction $x_p F_2^{D(3)}(x_p, \beta, Q^2) \propto F_2(x = x_p, Q^2) / \log_{10}(Q^2/Q_0^2)$. Here, $Q_0^2 \approx 0.55 \text{ GeV}^2$ was taken from an analysis of the $F_2(x, Q^2)$ data from HERA [61]. This relation predicts similar W dependences for the diffractive and total cross sections which is in agreement with the data presented above. It also predicts different Q^2 dependences for $x_p F_2^{D(3)}$ and F_2 .

The Q^2 behaviour of the two structure functions is compared in Fig. 12 which shows $x_p F_2^{D(3)}(x_p, \beta, Q^2)$ (solid points) for fixed values of M_X and W and $F_2(x = x_p, Q^2)$ (open points). The $F_2(x = x_p, Q^2)$ values were obtained from our published data [19] by taking that measurement of $F_2(x, Q^2)$ with x closest to x_p and transporting it to $x = x_p$. For ease of comparison, F_2 has been multiplied by a constant factor of 0.06. The comparison shows that the two quantities have different evolution with Q^2 . For $M_X < 7.5 \text{ GeV}$, $x_p F_2^{D(3)}$ decreases with Q^2 while the structure function $F_2(x, Q^2)$ gradually rises with Q^2 . In Fig. 12 $x_p F_2^{D(3)}$ is also compared with $F_2(x = x_p, Q^2) / \log_{10}(Q^2/Q_0^2)$ (points marked as stars) as suggested by [60]. Here, the F_2 values were multiplied by a factor of 0.05 as obtained from a fit to the $x_p F_2^{D(3)}$ for $M_X = 2 \text{ GeV}$. The Q^2 evolution of the data at low M_X ($M_X < 3 \text{ GeV}$) is well described by this model. At larger M_X values there is a tendency for the data to lie above the BH prediction. We note that in the BEKW model this is understood as resulting from the logarithmic growth of the $(q\bar{q}g)$ contribution with Q^2 .

13 Summary and conclusion

The DIS diffractive cross section $d\sigma_{\gamma^*p \rightarrow XN}^{diff}/dM_X$, has been measured for $M_N < 5.5 \text{ GeV}$, $M_X < 15 \text{ GeV}$, $60 < W < 200 \text{ GeV}$ and $7 < Q^2 < 140 \text{ GeV}^2$. For fixed Q^2 the diffractive cross section rises rapidly with W . A fit of the W dependence by the form $d\sigma_{\gamma^*p \rightarrow XN}^{diff}(M_X, W, Q^2)/dM_X \propto$

$W^{a^{diff}}$ yielded $a^{diff} = 0.507 \pm 0.034(stat)_{-0.046}^{+0.155}(syst)$ which corresponds to a t -averaged pomeron trajectory of $\bar{\alpha}_p = 1.127 \pm 0.009(stat)_{-0.012}^{+0.039}(syst)$. The rise is faster than expected in Regge models using the intercept of the pomeron trajectory extracted from hadron-hadron scattering. The W dependence of the diffractive cross section, contrary to naïve expectations, is the same as that of the total virtual photon proton cross section. The diffractive contribution to the total cross section for $M_X < 15$ GeV, $M_N < 5.5$ GeV and $134 < W < 200$ GeV amounts to $13.2_{-0.7}^{+0.5}\%$ at $Q^2 = 8$ GeV² decreasing to $3.7_{-0.4}^{+0.3}\%$ at $Q^2 = 60$ GeV².

The analysis of the data in terms of the diffractive structure function $F_2^{D(3)}(x_p, \beta, Q^2)$ of the proton shows that $x_p F_2^{D(3)}$ rises as $x_p \rightarrow 0$. The data are consistent with the assumption that the diffractive structure function $F_2^{D(3)}$ factorizes into a term depending only on x_p and a structure function $F_2^{D(2)}$ which depends on (β, Q^2) . The rise of $x_p F_2^{D(3)}$ with x_p can be described as $x_p F_2^{D(3)} \propto (1/x_p)^n$ with $n = 0.253 \pm 0.017(stat)_{-0.023}^{+0.077}(syst)$. The data are also consistent with models which break factorization. The rise of $F_2^{D(3)}$ reflects the rise of $d\sigma_{\gamma^*p \rightarrow XN}^{diff}/dM_X$ with W . For fixed $M_X < 7.5$ GeV and fixed W , $x_p F_2^{D(3)}$ decreases slowly with Q^2 while for $M_X = 11$ GeV it is approximately constant.

The data have been compared with several partonic models of diffraction. Good agreement with the data can be achieved. The models provide a first glimpse of how the different components may build up the diffractive structure function. The Q^2 behaviour of $x_p F_2^{D(3)}(x_p, \beta, Q^2)$ is different from that of the proton structure function $F_2(x, Q^2)$, taken at $x = x_p$, which rises gradually with Q^2 . It is in broad agreement with the BH conjecture that $x_p F_2^{D(3)}(x_p, \beta, Q^2) \propto F_2(x = x_p, Q^2)/\log_{10}(Q^2/Q_0^2)$ where $Q_0^2 = 0.55$ GeV². Using the BEKW model at medium β the main contribution comes from transverse photons coupling to a $q\bar{q}$ system. The region $\beta < 0.2$ is dominated by $q\bar{q}g$ contributions. Longitudinal photons coupling to a $q\bar{q}$ system account for most of the data at $\beta > 0.8$. The transverse photon $q\bar{q}$ contribution, which is dominant, is of leading twist and has no substantial evolution with Q^2 .

The leading twist behaviour and the strong rise of $x_p F_2^{D(3)}$ as $x_p \rightarrow 0$ suggest a partonic process as a major production mechanism for diffractive scattering in DIS.

References

- [1] G. Alberi and G. Goggi, Phys. Reports, 74 (1981) 1.
K. Goulianos, Phys. Reports. 101 (1983) 169; Nucl. Phys. B, Proc. Suppl. 12 (1990) 110.
G. Giacomelli, University and INFN Bologna report DFUB 9-94 (1994) and 1994 Marshak Memorial Volume, "A Gift of Prophecy", ed. E.C.G. Sudarshan, p. 168.
- [2] N. Gribov, Sov. Phys. JETP 14 (1962) 478; *ibid.* 1395.
G.F. Chew and S. Frautschi, Phys. Rev. Lett. 7 (1961) 394.
- [3] R.D. Field and G. Fox, Nucl. Phys. B80 (1974) 367.
- [4] A.B. Kaidalov and K.A. Ter-Martirosyan, Nucl. Phys. B75 (1974) 471.
- [5] A. Donnachie and P.V. Landshoff, Nucl. Phys. B244 (1984) 322; Phys. Lett. B296 (1992) 227.
- [6] G. Ingelman and P. Schlein, Phys. Lett. B152 (1985) 256.

- [7] UA8 Collab., R. Bonino et al., Phys. Lett., B211 (1988) 239; A. Brandt et al., Phys. Lett. B297 (1992) 417.
- [8] ZEUS Collab., M. Derrick et al., Phys. Lett. B315 (1993) 481.
- [9] H1 Collab., T. Ahmed et al., Nucl. Phys. B429 (1994) 477.
- [10] ZEUS Collab., M. Derrick et al., Phys. Lett. B332 (1994) 228; *ibid.* B338 (1994) 483; J. Breitweg et al., Phys. Lett. B421 (1998) 36.
- [11] ZEUS Collab., M. Derrick et al., Z. Phys. C68 (1995) 569.
- [12] H1 Collab., T. Ahmed et al., Phys. Lett. B348 (1995) 681.
- [13] ZEUS Collab., M. Derrick et al., Z. Phys. C70 (1996) 391.
- [14] H1 Collab., C. Adloff et al., Z. Phys. C76 (1997) 613.
- [15] ZEUS Collab., J. Breitweg et al., Eur. Phys. J. C1 (1998) 81.
- [16] G. Ingelman and K. Janson-Prytz, Proc. Workshop "Physics at HERA", ed. W. Buchmüller and G. Ingelman, DESY 1992, Vol. 1, 233; G. Ingelman and K. Prytz, Z. Phys. C58 (1993) 285.
- [17] ZEUS Collab., M. Derrick et al., Phys. Lett. B316 (1993) 412; Z. Phys. C65 (1995) 379; *ibid.* C69 (1996) 607; J. Breitweg et al., Phys. Lett. B407 (1997) 432.
- [18] H1 Collab., I. Abt et al., Nucl. Phys. B407 (1993) 515; T. Ahmed et al., *ibid.* B439 (1995) 471; S. Aid et al., Nucl. Phys. B470 (1996) 3; C. Adloff et al., Nucl. Phys. B497 (1997) 3.
- [19] ZEUS Collab., J. Breitweg et al., Z. Phys. C72 (1996) 399.
- [20] ZEUS Collab., M. Derrick et al., Phys. Lett., B297 (1992) 404; B303 (1993) 183
The ZEUS Detector, Status Report 1993, ed. U. Holm.
- [21] A. Andresen et al., Nucl. Instr. Meth. A309 (1991) 101.
A. Bernstein et al., *ibid.* A336 (1993) 23.
A. Caldwell et al., *ibid.* A321 (1992) 356.
- [22] N. Harnew et al., Nucl. Instr. Meth. A279 (1989) 290.
B. Foster et al., Nucl. Phys. B(Proc. Suppl.) 32 (1993) 181 and Nucl. Inst. Meth. A338 (1994) 254.
- [23] A. Bamberger et al., Nucl. Instr. Meth. A401 (1997) 63.
- [24] ZEUS Collab., J. Breitweg et al., Z. Phys. C75 (1997) 421.
- [25] J. Andruszkow et al., DESY 92-066 (1992);
ZEUS Collab., M. Derrick et al., Z. Phys. C63 (1994) 391.
- [26] H. Abramowicz, A. Caldwell and R. Sinkus, Nucl. Inst. Meth. A356 (1995) 508.
- [27] G. Briskin, PhD Thesis, 1998, University of Tel Aviv.

- [28] S. Bentvelsen, J. Engelen and P. Kooijman, Proc. Workshop “Physics at HERA”, ed. W. Buchmüller and G. Ingelman, DESY 1992, Vol. 1,23.
K.C. Hoeger, *ibid.*, p.43.
- [29] F. Jacquet and A. Blondel, Proc. Study of an *ep* Facility for Europe, ed. U. Amaldi, DESY 79/48 (1979) 391.
- [30] GEANT 3.13: R. Brun et al., CERN DD/EE/84-1 (1987).
- [31] RAPGAP: H. Jung, Comp. Phys. Comm. 86 (1995) 147 and private communication.
- [32] V.N. Gribov and L.N. Lipatov, Sov. J. Nucl. Phys. 15 (1972) 438; *ibid.* 675.
L.N. Lipatov, Sov. J. Nucl. Phys. 20 (1975) 95.
Yu.L. Dokshitzer, Sov. Phys. JETP 46 (1977) 641.
G. Altarelli and G. Parisi, Nucl. Phys. B126 (1977) 298.
- [33] ARIADNE 4.0 Program Manual, L. Lönnblad, DESY-92-046 (1992).
- [34] B. Andersson et al., Phys. Rep. 97 (1983) 31.
- [35] JETSET 7.4: T. Sjöstrand, Comp. Phys. Comm. 82 (1994) 74.
- [36] ZEUS Collab., M. Derrick et al., Phys. Lett. B356 (1995) 601.
- [37] ZEUS Collab., M. Derrick et al., Phys. Lett. B380 (1996) 220.
- [38] H1 Collab., S. Aid et al., Nucl. Phys. B468 (1996) 3; C. Adloff et al., Z. Phys. C75 (1997) 607.
- [39] M. Kasprzak, PhD thesis, Warsaw University, DESY F35D-96-16 (1996).
- [40] A.H. Mueller, Phys. Rev. D2 (1970) 2963; *ibid.* D4 (1971) 150.
- [41] DJANGO: G. A. Schuler and H. Spiesberger, Proc. Workshop “Physics at HERA”, ed. W. Buchmüller and G. Ingelman, DESY 1992, Vol. 3, 1419.
- [42] HERACLES 4.1: A. Kwiatkowski, H. Spiesberger and H.J. Möhring, Proc. Workshop “Physics at HERA”, ed. W. Buchmüller and G. Ingelman, DESY 1992, Vol. 3, 1294; A. Kwiatkowski, H. Spiesberger and H.J. Möhring, Z. Phys. C50 (1991) 165.
- [43] LEPTO 6.5 G. Ingelman, A. Edin and J. Rathsman, Comp. Phys. Comm. 101 (1997) 108.
- [44] A. D. Martin, W.J. Stirling and R.G. Roberts, Phys. Lett. B306 (1993) 145.
- [45] J. Ellis and G. Ross, Phys. Lett. B384 (1996) 293.
- [46] R.P. Feynman, “Photon-Hadron Interactions”, Benjamin, N.Y. (1972), lectures 50 - 54.
- [47] N. Pavel, Habilitation thesis, 1994, University of Hamburg, DESY 95-147 (1995).
- [48] M. Kuhlen, Habilitation thesis, 1998, University of Hamburg.
- [49] CDF Collab., F. Abe et al., Phys. Rev. D50 (1994) 5535.

- [50] N.N. Nikolaev and B.G. Zakharov, *Z. Phys.* C53 (1992) 331; M. Genovese, N.N. Nikolaev and B.G. Zakharov, *JETP* 81 (1995) 625; M. Bertini, M. Genovese, N.N. Nikolaev, A.V.Pronyaev and B.G. Zakharov, *Phys. Lett. B*(1998) 238.
- [51] POMPYT 1.0: P. Bruni and G. Ingelman, *Proc. Europhysics Conf. on HEP, Marseilles 1993*, 595.
- [52] A. Donnachie and P.V. Landshoff, *Phys. Lett.* B191 (1987) 309; *Nucl. Phys.* B303 (1988) 634.
- [53] H. Beier, PhD thesis, University of Hamburg, DESY F35D-97-06.
- [54] J. Bartels, J. Ellis, H. Kowalski and M. Wüsthoff, CERN-TH/98-67, DESY 98-034, DTP 98-02 and hep-ph/9803497.
- [55] L.N. Hand, *Phys. Rev.* 129 (1963) 1834.
S.D. Drell and J.D. Walecka, *Ann. Phys. (N.Y.)* 28 (1964) 18.
F.J. Gilman, *Phys. Rev.* 167 (1968) 1365.
- [56] V. Blobel, Minimization program MINGUS.
- [57] J. Cudell, K. Kang and S.K. Kim, Brown-HET-1060 and hep-ph/9701312.
- [58] A.H. Mueller, Talk given at “Interplay between Soft and Hard Interactions in Deep Inelastic Scattering”, Heidelberg, 1997, hep-ph/9710531 (1997).
- [59] S.D. Brodsky, A. Hebecker and E. Quack, *Phys. Rev.* D55 (1997) 2584.
- [60] W. Buchmüller, *Phys. Lett.* B353 (1995) 335; W. Buchmüller and A. Hebecker, *Nucl. Phys.* B476 (1996) 203.
- [61] W. Buchmüller and D. Haidt, DESY 96-087; D. Haidt, *Proc. Workshop on DIS, Chicago, 1997*, AIP 1997, p.386.
- [62] J.D. Bjorken, *Proc. Int. Symp. Electron and Photon Interactions at High Energies, Cornell, 1971*, p. 282.
J.D. Bjorken, J. Kogut and D. Soper, *Phys. Rev.* D3 (1971) 1382.
J.D. Bjorken and J. Kogut, *Phys. Rev.* D8 (1973) 1341.
- [63] A. Donnachie and P.V. Landshoff, *Phys. Lett.* B191 (1987) 309.
- [64] M. Wüsthoff, PhD thesis, University of Hamburg, DESY 95-166.
- [65] E. Gotsman, E. Levin and U. Maor, *Nucl. Phys.* B493 (1997) 354.
- [66] L.N. Lipatov, *Sov. J. Nucl. Phys.* 23 (1976) 338.
Y.Y. Balitsky and L.N. Lipatov, *Sov. J. Nucl. Phys.* 28 (1978) 822.
E.A. Kuraev, L.N. Lipatov and V.S. Fadin, *Sov. Phys. JETP* 45 (1977) 199.
- [67] A. Bialas and R. Peschanski, *Phys. Lett.* B387 (1996) 405; A. Bialas, R. Peschanski and Ch. Royon, *Phys. Rev.* D57 (1998) 6899.

- [68] M. Ryskin, *Sov. J. Nucl. Phys.* 52 (1990) 529.
N.N. Nikolaev and B.G. Zakharov, *Phys. Lett.* B332 (1994) 177.
E.M. Levin and M. Wüsthoff, *Phys. Rev.* D50 (1994) 4306.
S.J. Brodsky et al., *Phys. Rev.* D50 (1994) 3134.
J. Bartels, H. Lotter and M. Wüsthoff, *Phys. Lett.* B379 (1996) 239; Erratum *ibid.*
B382 (1996) 449.

Table 1: Cross section for diffractive scattering via $\gamma^*p \rightarrow XN$, where N is the proton or dissociated nucleonic system with mass $M_N < 5.5$ GeV as a function of M_X, Q^2 and W . The statistical and systematic errors are given. The overall normalization uncertainty of $\pm 2\%$ is not included.

M_X (GeV)	Q^2 (GeV ²)	W (GeV)	$d\sigma_{\gamma^*p \rightarrow XN}^{diff}/dM_X$	\pm stat (nb/GeV)	\pm syst
2.0	8.0	66.7	138.6	± 9.5	+11.8 -11.6
2.0	8.0	81.8	153.8	± 10.1	+11.8 -12.2
2.0	8.0	99.8	180.0	± 11.7	+13.6 -11.7
2.0	8.0	122.1	192.3	± 13.4	+19.6 -13.3
2.0	8.0	148.6	221.9	± 13.2	+20.2 -16.5
2.0	8.0	181.5	219.9	± 13.9	+22.2 -17.5
5.0	8.0	66.9	120.3	± 7.9	+11.5 -27.1
5.0	8.0	81.6	127.9	± 7.0	+13.1 -21.2
5.0	8.0	99.9	139.8	± 7.5	+12.1 -17.7
5.0	8.0	121.9	162.8	± 8.2	+8.0 -14.0
5.0	8.0	148.9	175.4	± 8.8	+20.6 -12.4
5.0	8.0	181.7	198.4	± 10.0	+11.0 -13.6
11.0	8.0	121.7	68.9	± 4.2	+5.9 -22.9
11.0	8.0	149.1	74.5	± 4.4	+7.0 -16.1
11.0	8.0	181.6	78.4	± 4.8	+2.7 -12.9
2.0	14.0	67.2	48.0	± 3.6	+3.7 -6.1
2.0	14.0	81.5	48.9	± 4.1	+9.2 -4.2
2.0	14.0	100.0	58.1	± 4.8	+7.2 -4.0
2.0	14.0	121.6	60.0	± 5.5	+10.6 -4.4
2.0	14.0	148.5	55.2	± 5.7	+15.6 -5.0
2.0	14.0	181.8	76.7	± 5.3	+6.9 -7.1
5.0	14.0	67.0	52.3	± 3.7	+3.7 -12.7
5.0	14.0	81.7	61.4	± 3.2	+5.5 -11.9
5.0	14.0	99.9	73.5	± 3.7	+3.8 -9.5
5.0	14.0	121.7	76.9	± 3.8	+4.7 -7.5
5.0	14.0	148.9	83.7	± 4.1	+9.1 -5.9
5.0	14.0	182.0	83.8	± 4.3	+12.0 -3.3
11.0	14.0	149.1	40.0	± 2.2	+3.7 -9.7
11.0	14.0	181.6	43.2	± 2.4	+3.7 -6.2
2.0	27.0	67.2	9.1	± 1.4	+2.0 -1.8
2.0	27.0	82.2	13.4	± 2.0	+2.8 -1.7
2.0	27.0	99.4	12.5	± 2.3	+2.6 -1.3
2.0	27.0	121.4	16.0	± 2.6	+3.4 -1.6
2.0	27.0	148.9	20.5	± 3.2	+2.8 -2.7
2.0	27.0	182.0	24.3	± 3.5	+1.7 -3.4
5.0	27.0	81.7	21.1	± 2.0	+3.2 -5.4
5.0	27.0	99.5	23.6	± 2.0	+2.0 -3.6
5.0	27.0	121.8	26.4	± 2.3	+3.2 -3.0
5.0	27.0	149.2	32.8	± 2.6	+1.6 -3.1
5.0	27.0	181.1	33.4	± 2.7	+4.1 -2.7
11.0	27.0	148.9	19.6	± 1.6	+1.6 -4.4
11.0	27.0	181.5	25.8	± 2.0	+0.6 -4.1
2.0	60.0	81.2	0.8	± 0.3	+0.6 -0.3
2.0	60.0	101.1	1.9	± 0.5	+0.2 -0.6
2.0	60.0	122.5	1.4	± 0.4	+0.4 -0.2
2.0	60.0	148.8	2.1	± 0.5	+1.2 -0.3
2.0	60.0	180.2	4.5	± 1.0	+0.4 -2.7
5.0	60.0	99.4	4.2	± 0.7	+0.7 -1.7
5.0	60.0	122.5	4.4	± 0.6	+1.0 -1.1
5.0	60.0	149.2	3.9	± 0.7	+1.5 -0.6
5.0	60.0	182.2	6.1	± 0.8	+1.2 -0.6
11.0	60.0	148.7	5.8	± 0.8	+1.0 -1.7
11.0	60.0	181.6	7.8	± 0.8	+0.3 -1.3

Table 2: The diffractive structure function multiplied by $x_P, x_P F_2^{D(3)}(x_P, \beta, Q^2)$, for diffractive scattering via $\gamma^*p \rightarrow XN$, where N is a nucleonic system with mass $M_N < 5.5$ GeV as a function of x_P, β and Q^2 . The statistical and systematic errors are given. The overall normalization uncertainty of $\pm 2\%$ is not included.

x_P	β	Q^2 (GeV ²)	$x_P F_2^{D(3)}$	\pm stat	\pm syst
0.00269	0.667	8.0	0.0297	\pm 0.0020	+0.0025 -0.0025
0.00179	0.667	8.0	0.0329	\pm 0.0022	+0.0025 -0.0025
0.00120	0.667	8.0	0.0385	\pm 0.0025	+0.0029 -0.0025
0.00081	0.667	8.0	0.0411	\pm 0.0029	+0.0042 -0.0028
0.00054	0.667	8.0	0.0475	\pm 0.0028	+0.0043 -0.0035
0.00036	0.667	8.0	0.0471	\pm 0.0030	+0.0047 -0.0037
0.00735	0.242	8.0	0.0284	\pm 0.0019	+0.0027 -0.0064
0.00495	0.242	8.0	0.0301	\pm 0.0016	+0.0031 -0.0056
0.00330	0.242	8.0	0.0329	\pm 0.0018	+0.0048 -0.0042
0.00222	0.242	8.0	0.0383	\pm 0.0019	+0.0019 -0.0033
0.00149	0.242	8.0	0.0413	\pm 0.0021	+0.0049 -0.0029
0.00100	0.242	8.0	0.0467	\pm 0.0023	+0.0026 -0.0032
0.00871	0.062	8.0	0.0288	\pm 0.0018	+0.0025 -0.0096
0.00580	0.062	8.0	0.0312	\pm 0.0018	+0.0029 -0.0067
0.00391	0.062	8.0	0.0328	\pm 0.0020	+0.0011 -0.0054
0.00398	0.778	14.0	0.0270	\pm 0.0020	+0.0021 -0.0034
0.00270	0.778	14.0	0.0275	\pm 0.0023	+0.0052 -0.0023
0.00180	0.778	14.0	0.0327	\pm 0.0027	+0.0041 -0.0022
0.00122	0.778	14.0	0.0337	\pm 0.0031	+0.0060 -0.0025
0.00082	0.778	14.0	0.0310	\pm 0.0032	+0.0087 -0.0028
0.00054	0.778	14.0	0.0431	\pm 0.0030	+0.0039 -0.0040
0.00866	0.359	14.0	0.0255	\pm 0.0018	+0.0025 -0.0062
0.00583	0.359	14.0	0.0300	\pm 0.0016	+0.0027 -0.0058
0.00390	0.359	14.0	0.0358	\pm 0.0018	+0.0018 -0.0046
0.00263	0.359	14.0	0.0375	\pm 0.0018	+0.0023 -0.0036
0.00176	0.359	14.0	0.0408	\pm 0.0020	+0.0044 -0.0029
0.00118	0.359	14.0	0.0408	\pm 0.0021	+0.0059 -0.0016
0.00607	0.104	14.0	0.0306	\pm 0.0017	+0.0028 -0.0074
0.00409	0.104	14.0	0.0331	\pm 0.0018	+0.0028 -0.0048
0.00682	0.871	27.0	0.0172	\pm 0.0027	+0.0038 -0.0033
0.00457	0.871	27.0	0.0251	\pm 0.0037	+0.0052 -0.0032
0.00313	0.871	27.0	0.0233	\pm 0.0043	+0.0048 -0.0024
0.00210	0.871	27.0	0.0299	\pm 0.0049	+0.0063 -0.0031
0.00140	0.871	27.0	0.0382	\pm 0.0059	+0.0053 -0.0050
0.00093	0.871	27.0	0.0453	\pm 0.0066	+0.0031 -0.0063
0.00776	0.519	27.0	0.0265	\pm 0.0026	+0.0040 -0.0068
0.00524	0.519	27.0	0.0296	\pm 0.0025	+0.0025 -0.0045
0.00350	0.519	27.0	0.0331	\pm 0.0029	+0.0041 -0.0037
0.00233	0.519	27.0	0.0411	\pm 0.0032	+0.0020 -0.0039
0.00158	0.519	27.0	0.0418	\pm 0.0034	+0.0051 -0.0034
0.00667	0.182	27.0	0.0318	\pm 0.0026	+0.0026 -0.0071
0.00449	0.182	27.0	0.0417	\pm 0.0032	+0.0010 -0.0067
0.00961	0.938	60.0	0.0073	\pm 0.0023	+0.0052 -0.0026
0.00622	0.938	60.0	0.0167	\pm 0.0045	+0.0017 -0.0053
0.00425	0.938	60.0	0.0119	\pm 0.0032	+0.0033 -0.0021
0.00288	0.938	60.0	0.0178	\pm 0.0046	+0.0106 -0.0027
0.00197	0.938	60.0	0.0386	\pm 0.0089	+0.0035 -0.0230
0.00856	0.706	60.0	0.0191	\pm 0.0030	+0.0031 -0.0079
0.00564	0.706	60.0	0.0202	\pm 0.0029	+0.0045 -0.0049
0.00381	0.706	60.0	0.0179	\pm 0.0032	+0.0068 -0.0026
0.00255	0.706	60.0	0.0276	\pm 0.0036	+0.0055 -0.0028
0.00817	0.331	60.0	0.0258	\pm 0.0034	+0.0043 -0.0074
0.00548	0.331	60.0	0.0345	\pm 0.0036	+0.0014 -0.0057

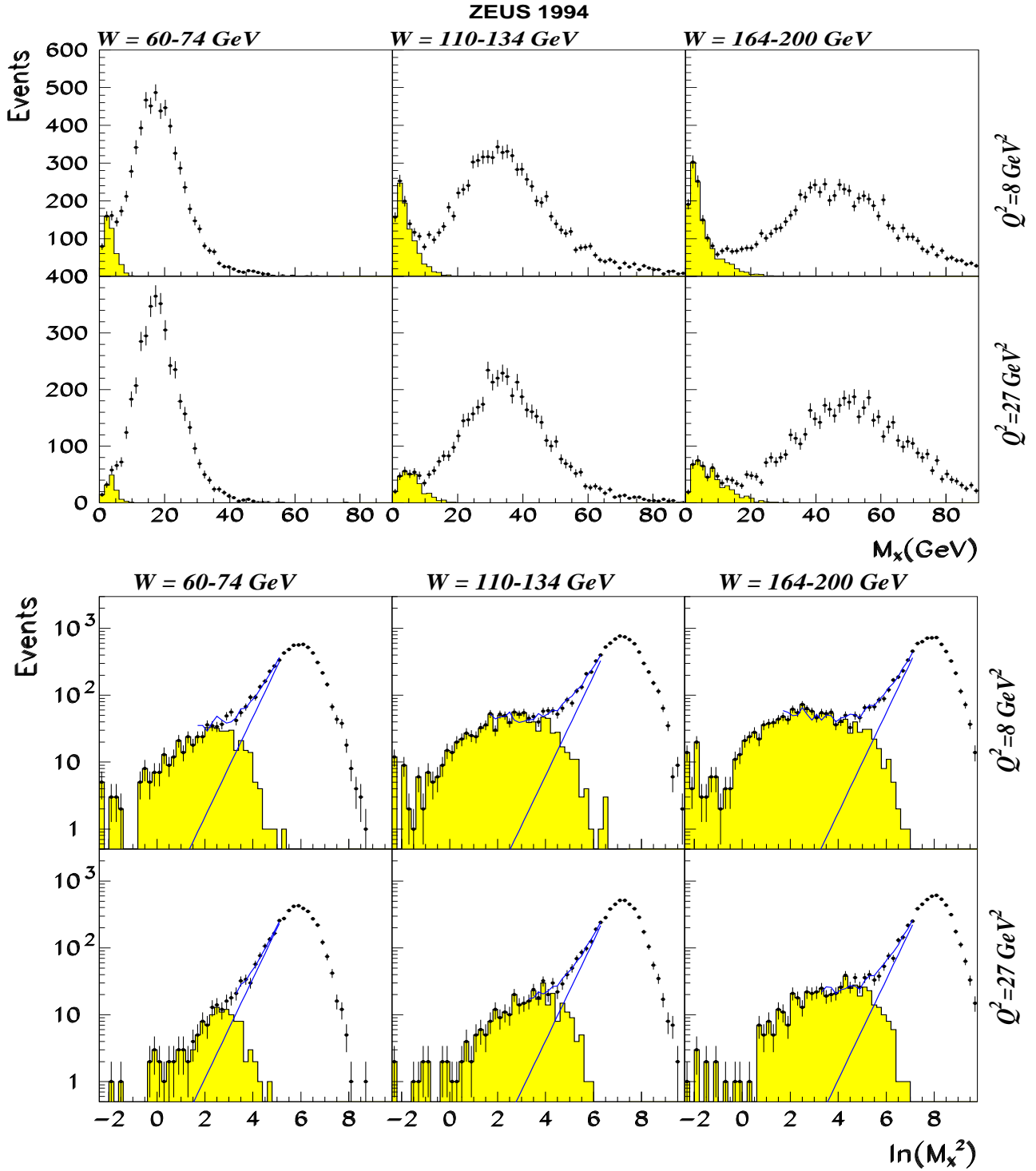


Figure 1: Reaction $\gamma^*p \rightarrow X + anything$, where X is the system observed in the detector. Top: Distributions of M_X , the corrected mass of the system X . The distributions are not corrected for acceptance effects. The shaded histograms show the distributions of events with $\eta_{max} < 1.5$. Bottom: Same distributions as above presented in terms of $\ln M_X^2$. The straight lines give the nondiffractive contributions as obtained from the fits. The upper curves show the fit results for the sum of the diffractive and nondiffractive contributions.

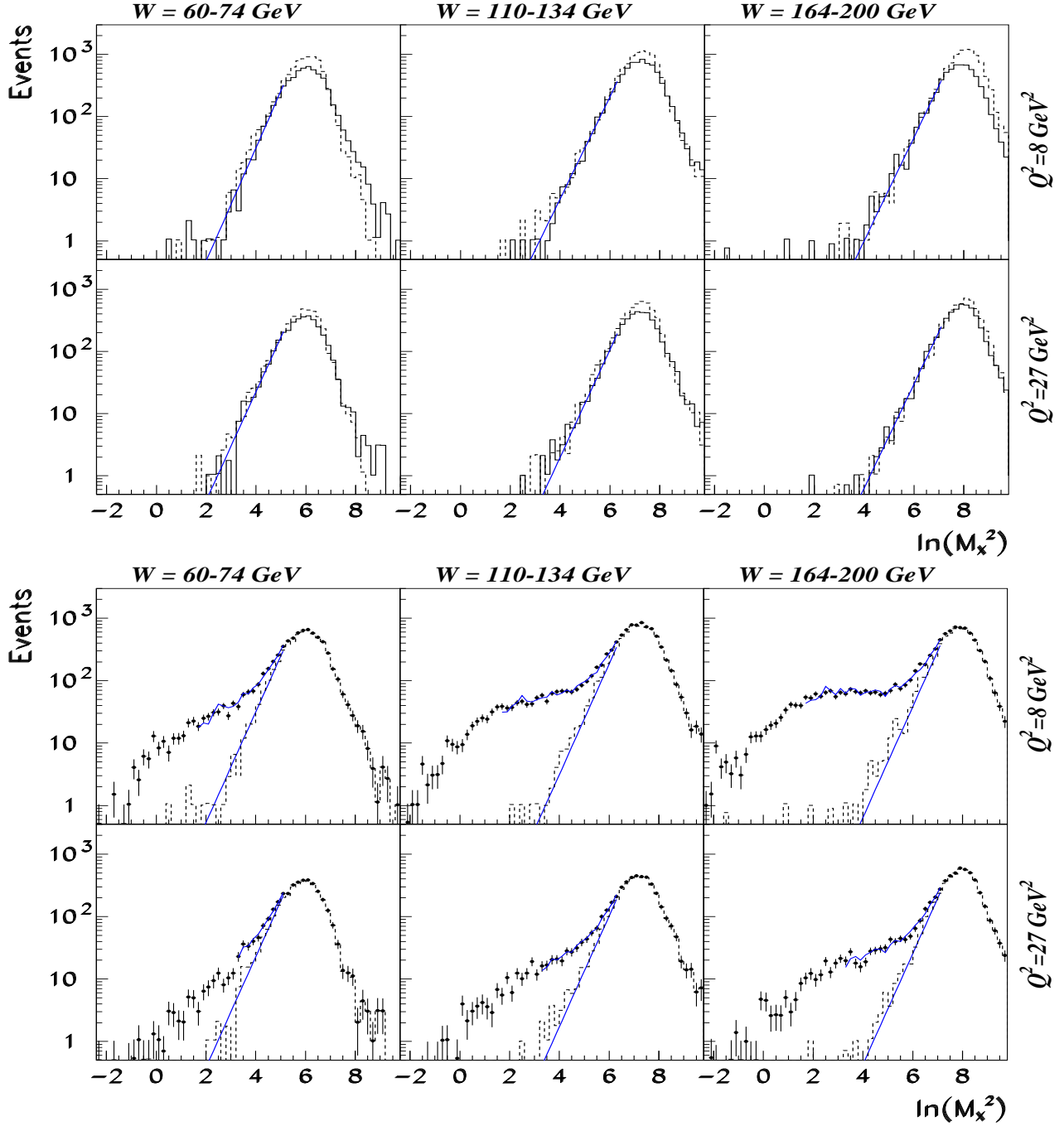


Figure 2: Reaction $\gamma^*p \rightarrow X + \text{anything}$, where X is the system observed in the detector. Top: Distributions in $\ln M_X^2$ as predicted by ARIADNE for the nondiffractive contribution at the generator level (solid histograms) and detector level (dashed histograms) for the W intervals and Q^2 values indicated. The straight lines show the results of the fits to the distributions at the detector level. Bottom: Distributions in $\ln M_X^2$ for the sum of the diffractive and nondiffractive contributions as predicted at the detector level by RAPGAP plus ARIADNE (points with error bars) and for the nondiffractive contribution alone (dashed histograms). The straight lines show the results for the nondiffractive contribution obtained from fitting the sum of the diffractive and nondiffractive contributions with b_{nom}^{MC} . The upper curves show the fit results for the sum of the diffractive and nondiffractive contributions.

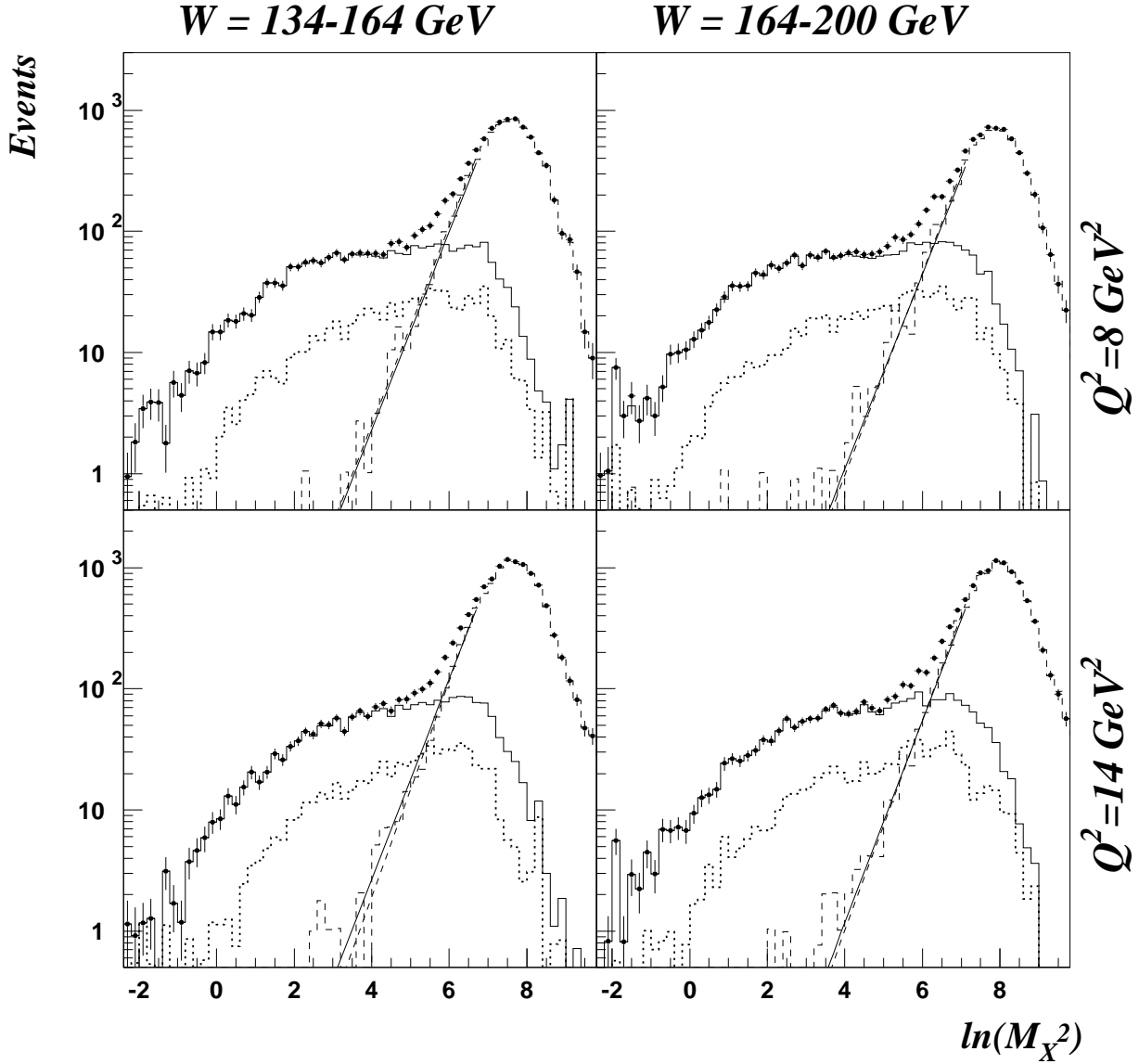


Figure 3: Reaction $\gamma^*p \rightarrow X + \text{anything}$, where X is the system observed in the detector. Shown are distributions of $\ln M_X^2$ at the detector level. The dotted histograms show the diffractive contributions from $\gamma^*p \rightarrow XN^{dissoc}$ as predicted by EPSOFT. The solid histograms show the sum of the diffractive contributions from $\gamma^*p \rightarrow XN^{dissoc}$ and $\gamma^*p \rightarrow Xp$ (the latter as predicted by RAPGAP). The dashed histograms show the nondiffractive contributions as predicted by ARIADNE. The points with error bars show the sum of the diffractive and the nondiffractive contributions. The dashed straight lines show the fits performed to the nondiffractive contributions alone. The straight lines show the results for the nondiffractive contribution from fitting the sum of the diffractive and nondiffractive contributions with $b^{MC(pN)}$.

ZEUS 1994

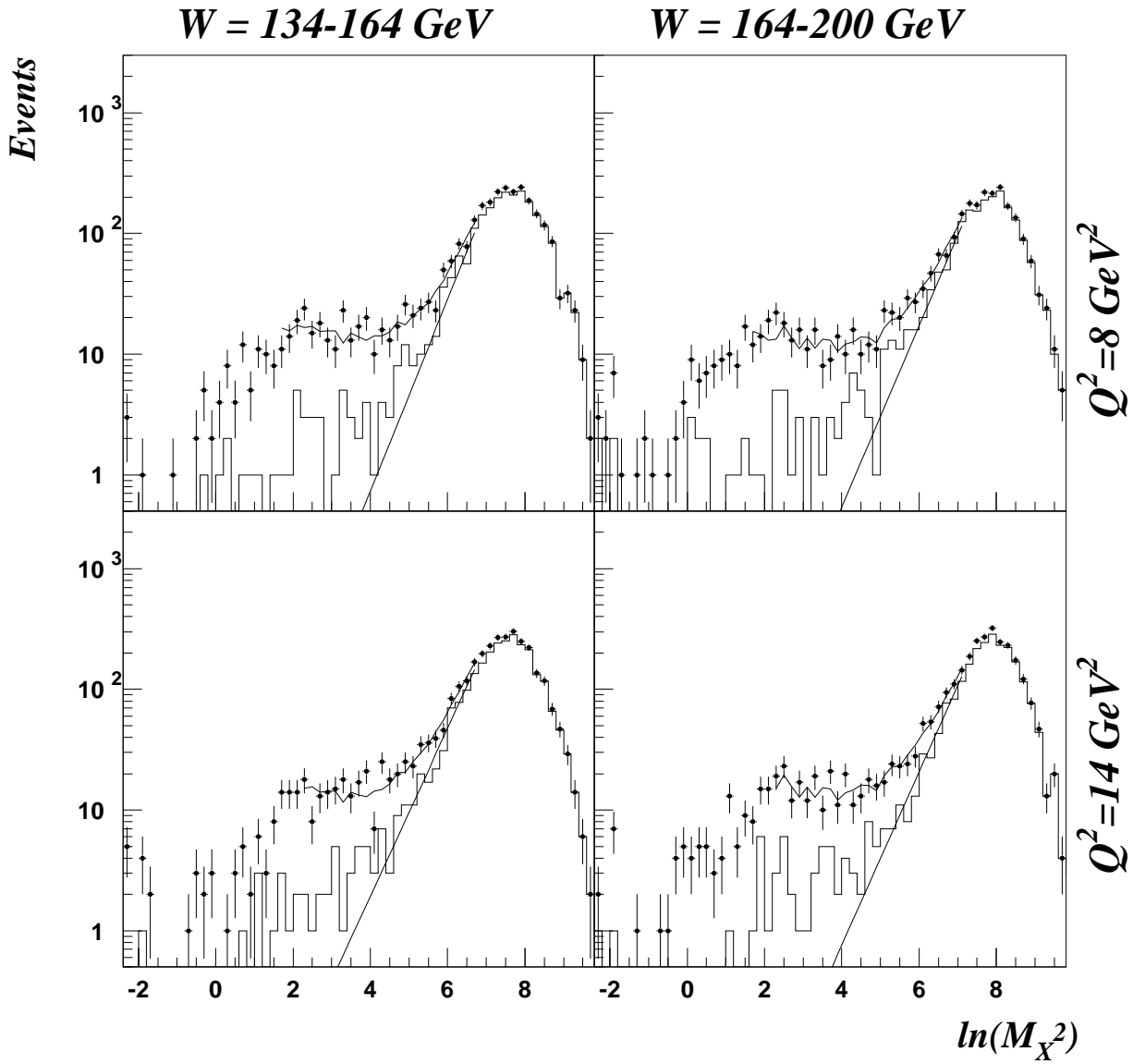


Figure 4: Reaction $\gamma^*p \rightarrow X + \text{anything}$, where X is the system observed in the detector. Distributions in $\ln M_X^2$ for data. The straight lines give the nondiffractive contributions and the upper curves the sum of the diffractive and nondiffractive contributions as obtained from the fits. The solid histograms show the distributions for events with a PRT signal.

ZEUS 1994

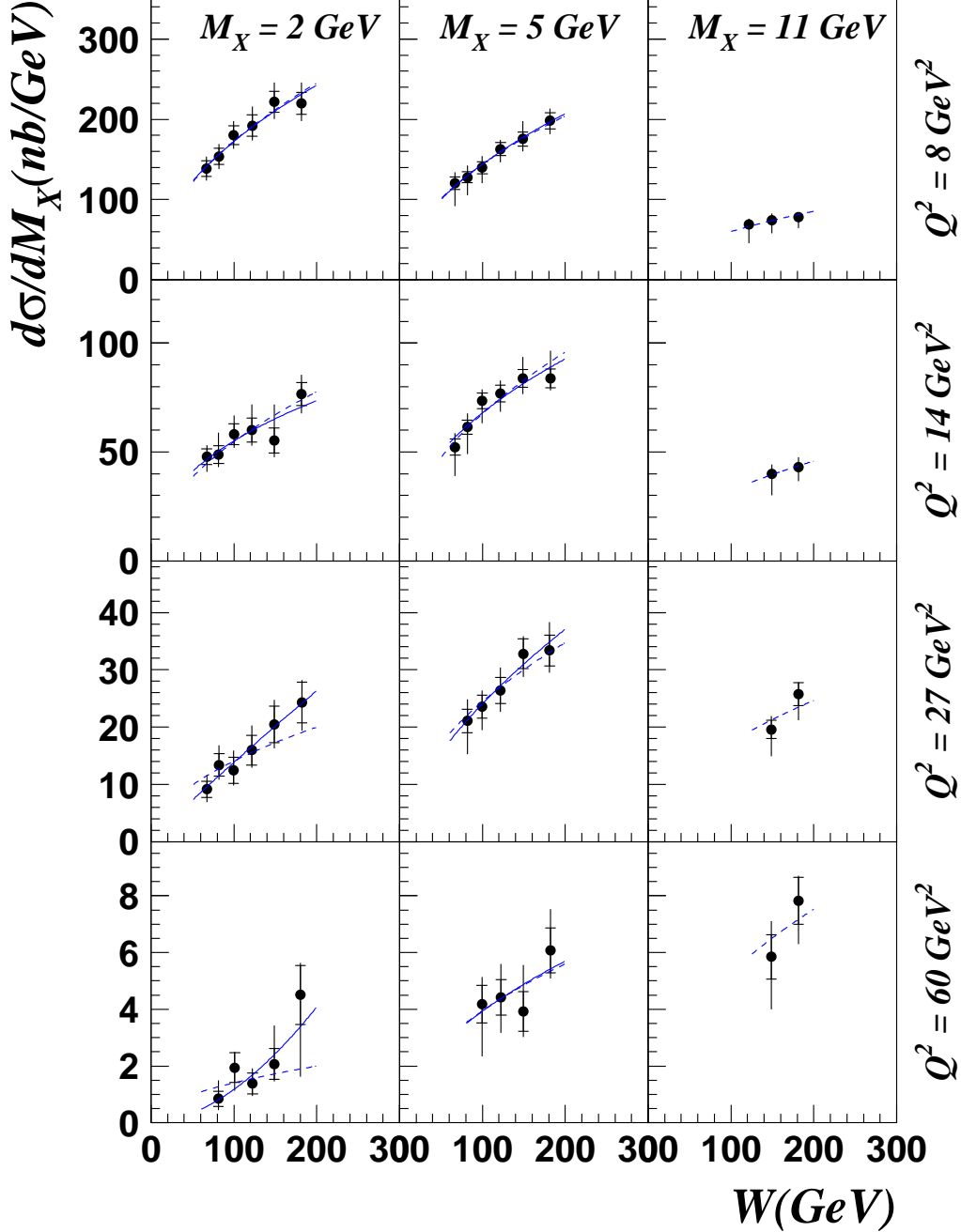


Figure 5: The differential cross sections $d\sigma_{\gamma^*p \rightarrow XN}^{diff}/dM_X$, $M_N < 5.5 \text{ GeV}$, as a function of W at average values of $M_X = 2, 5, 11 \text{ GeV}$, $Q^2 = 8, 13, 27, 60 \text{ GeV}^2$. The inner error bars show the statistical errors and the full bars the statistical and systematic errors added in quadrature. The overall normalization uncertainty of 2% is not included. The solid curves show the result from fitting the diffractive cross section for each (W, Q^2) bin separately using the form $d\sigma_{\gamma^*p \rightarrow XN}^{diff}/dM_X \propto (W^2)^{a^{diff}}$ where a^{diff} and the normalization constants were treated as free parameters. The dashed curves show the result from the fit where a^{diff} was assumed to be the same for all (W, Q^2) bins.

ZEUS 1994

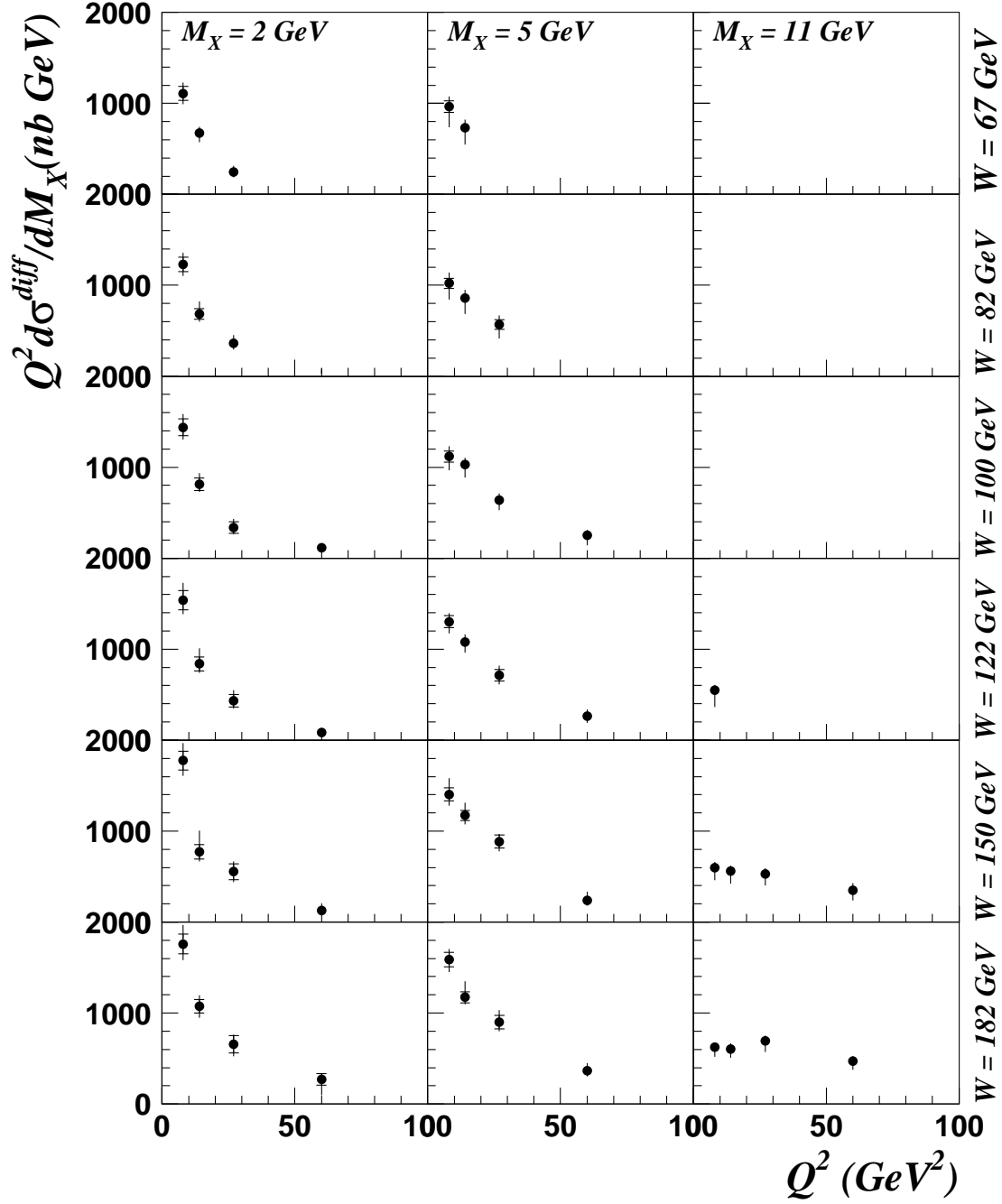


Figure 6: The diffractive differential cross section for $\gamma^*p \rightarrow XN$, $M_N < 5.5 \text{ GeV}$, multiplied by Q^2 , $Q^2 d\sigma^{diff}(\gamma^*p \rightarrow XN)/dM_X$, as a function of Q^2 for the values of M_X and W indicated. The inner error bars show the statistical errors and the full bars the statistical and systematic errors added in quadrature.

ZEUS 1994

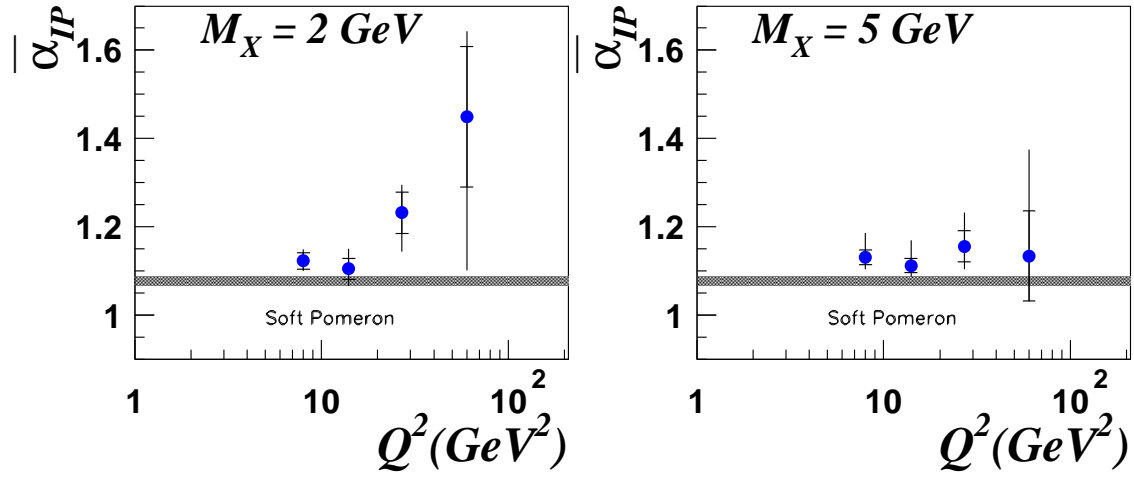


Figure 7: The parameter $\overline{\alpha_p}$ obtained from the fits versus Q^2 for $M_X = 2$ and 5 GeV . The inner error bars show the statistical errors and the full bars the statistical and systematic errors added in quadrature. The result for a soft pomeron is indicated by the heavy horizontal band.

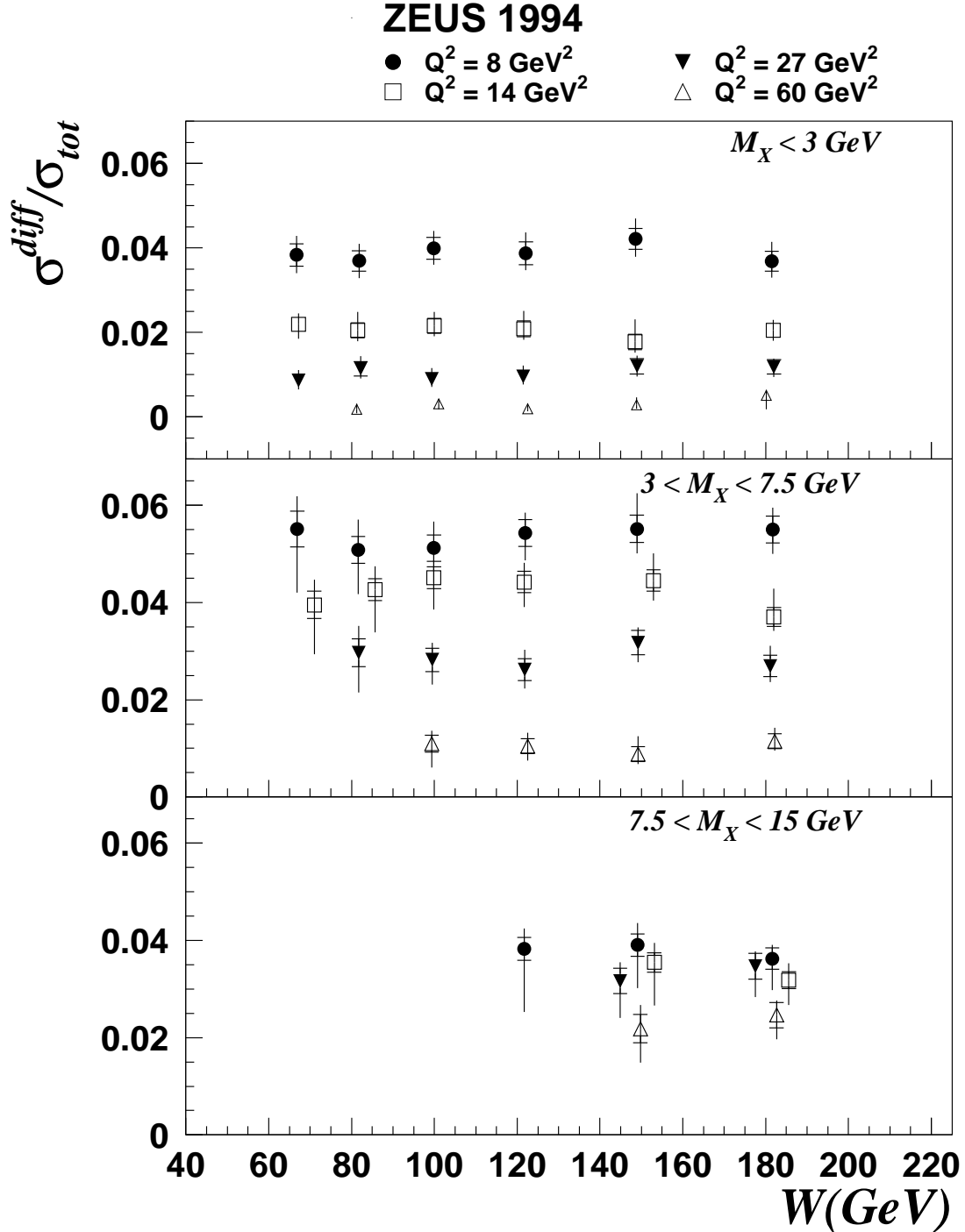


Figure 8: The ratio of the diffractive cross section, integrated over the M_X intervals indicated, $\sigma^{diff} = \int_{M_a}^{M_b} dM_X \sigma_{\gamma^* p \rightarrow XN}^{diff}$, for $M_N < 5.5 \text{ GeV}$, to the total cross section for virtual photon proton scattering, $r_{tot}^{diff} = \sigma^{diff} / \sigma_{\gamma^* p}^{tot}$, as a function of W for the M_X intervals and Q^2 values indicated. $\sigma_{tot}^{\gamma^* p}$ was taken from our F_2 measurements using the 1994 data [19]. The inner error bars show the statistical errors and the full bars the statistical and systematic errors added in quadrature.

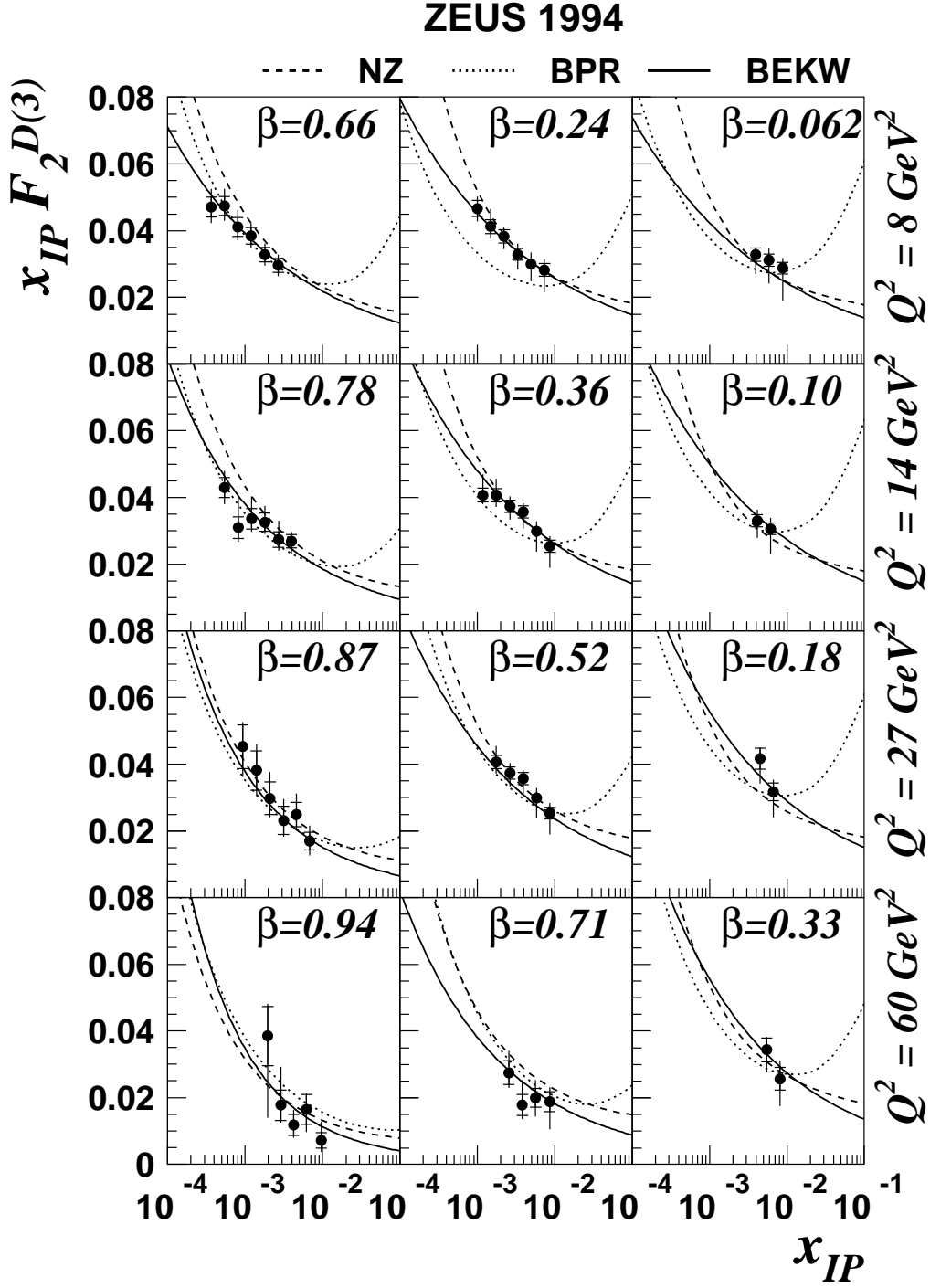


Figure 9: The diffractive structure function of the proton multiplied by x_{IP} , $x_{IP} F_2^{D(3)}$, as a function of x_{IP} from this analysis (solid points). The inner error bars show the statistical errors and the full bars the statistical and systematic errors added in quadrature. The curves show the results from the models of Nikolaev and Zhakarov (NZ), Bialas, Peschanski and Royon (BPR) and Bartels, Ellis, Kowalski and Wüsthoff (BEKW).

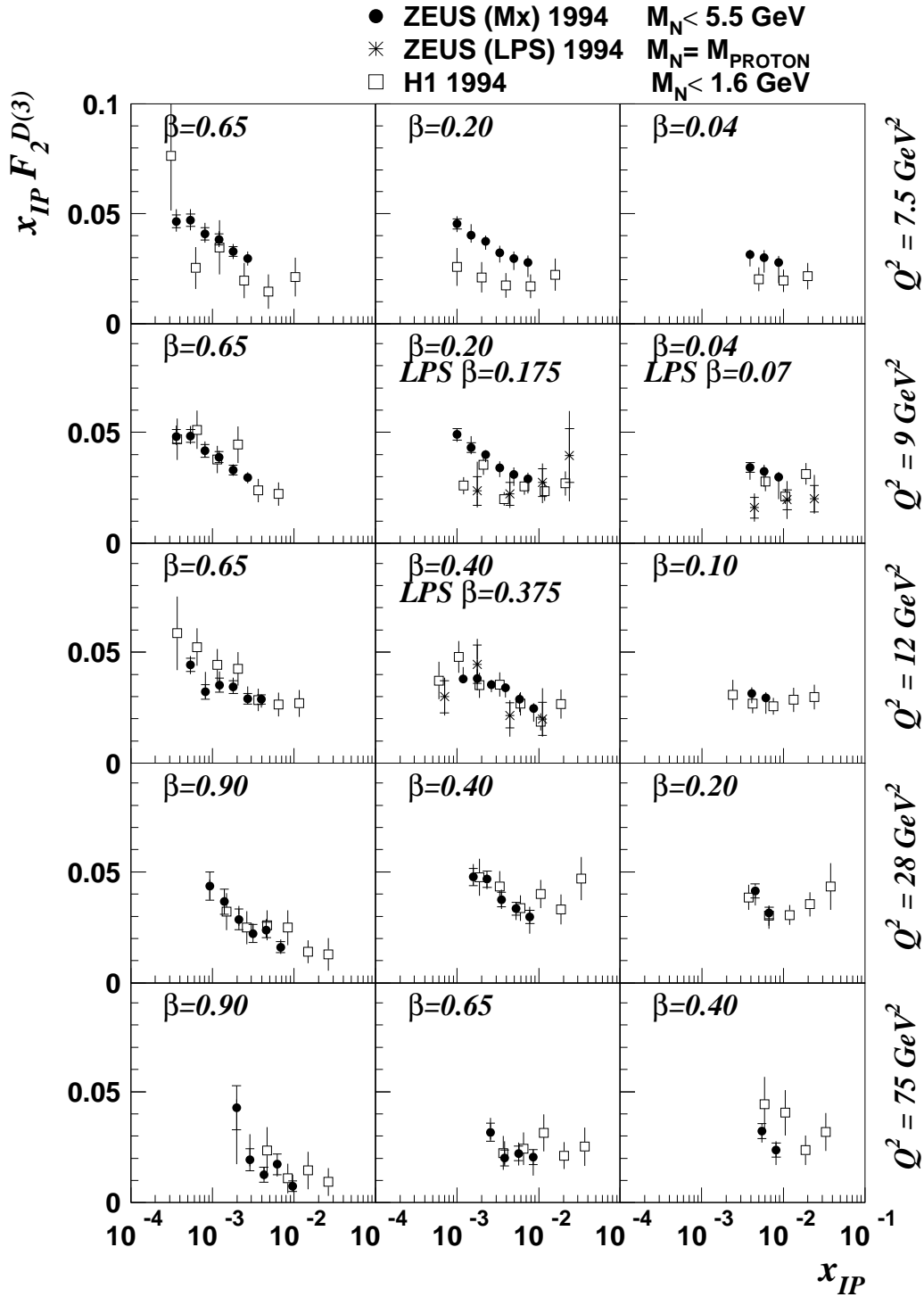


Figure 10: The diffractive structure function of the proton for $\gamma^*p \rightarrow XN$, $M_N < 5.5 \text{ GeV}$, multiplied by x_P , $x_P F_2^{D(3)}(x_P, \beta, Q^2)$, from this analysis (solid points) compared with the results from our previous LPS measurement obtained with an identified proton for $\gamma^*p \rightarrow Xp$ (stars) and from a subsample of the H1 data (open points) for $\gamma^*p \rightarrow XN$, $M_N < 1.6 \text{ GeV}$. For ease of comparison the results from this analysis are scaled to (β, Q^2) values used by H1. The data points from this experiment shown for $Q^2 = 7.5$ and 9 GeV^2 are those obtained at $Q^2 = 8 \text{ GeV}^2$ shifted to $Q^2 = 7.5$ and 9 GeV^2 . The LPS data are given for slightly different β and Q^2 values.

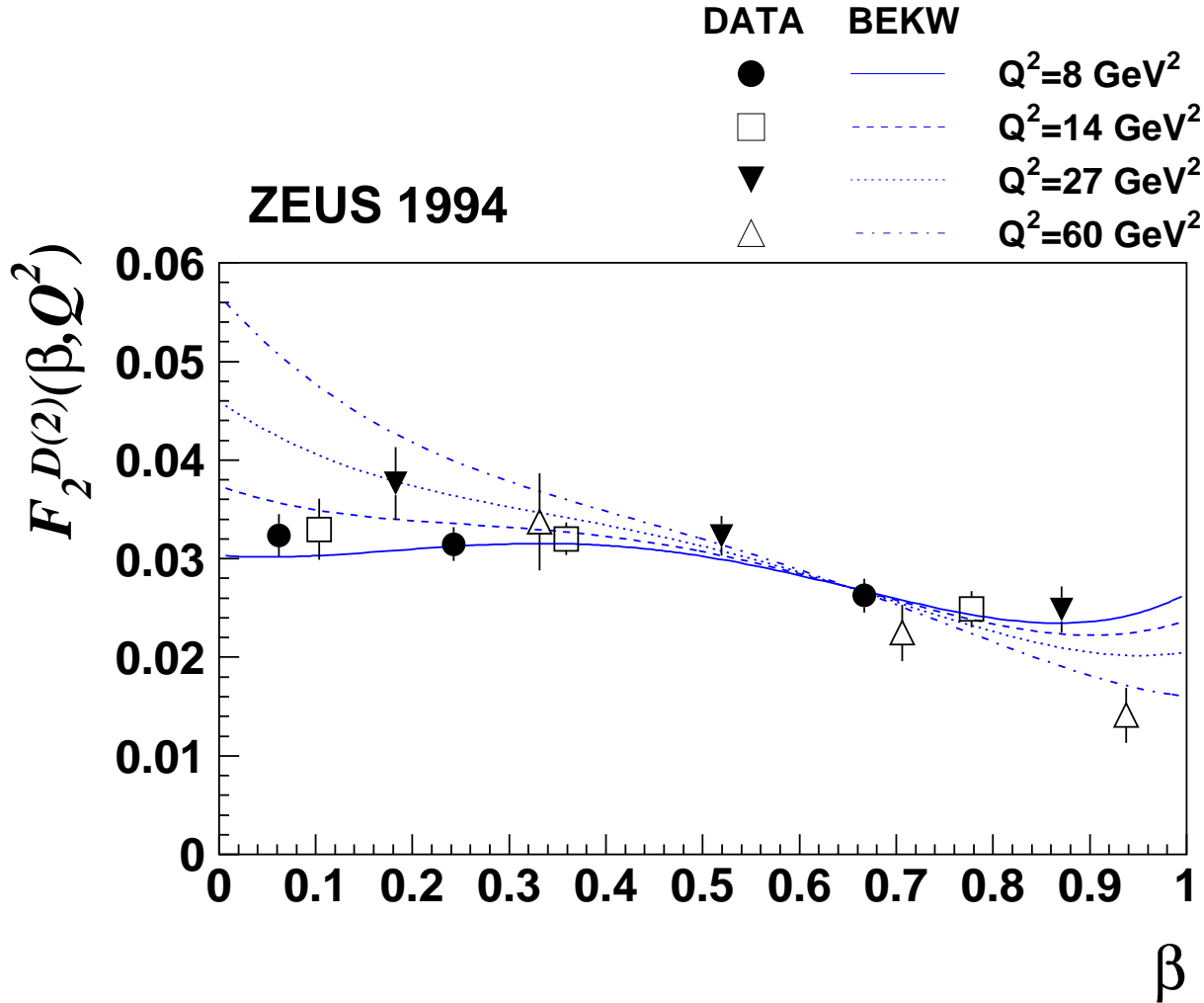


Figure 11: The structure function $F_2^{D(2)}(\beta, Q^2)$ for $\gamma^*p \rightarrow XN, M_N < 5.5 \text{ GeV}$, for the Q^2 values indicated, as a function of β as extracted from a fit to the measured $x_p F_2^{D(3)}$ values, see text. The error bars show the statistical and systematic errors added in quadrature. The curves show the fit results obtained with the BEKW model discussed in the text.

ZEUS 1994

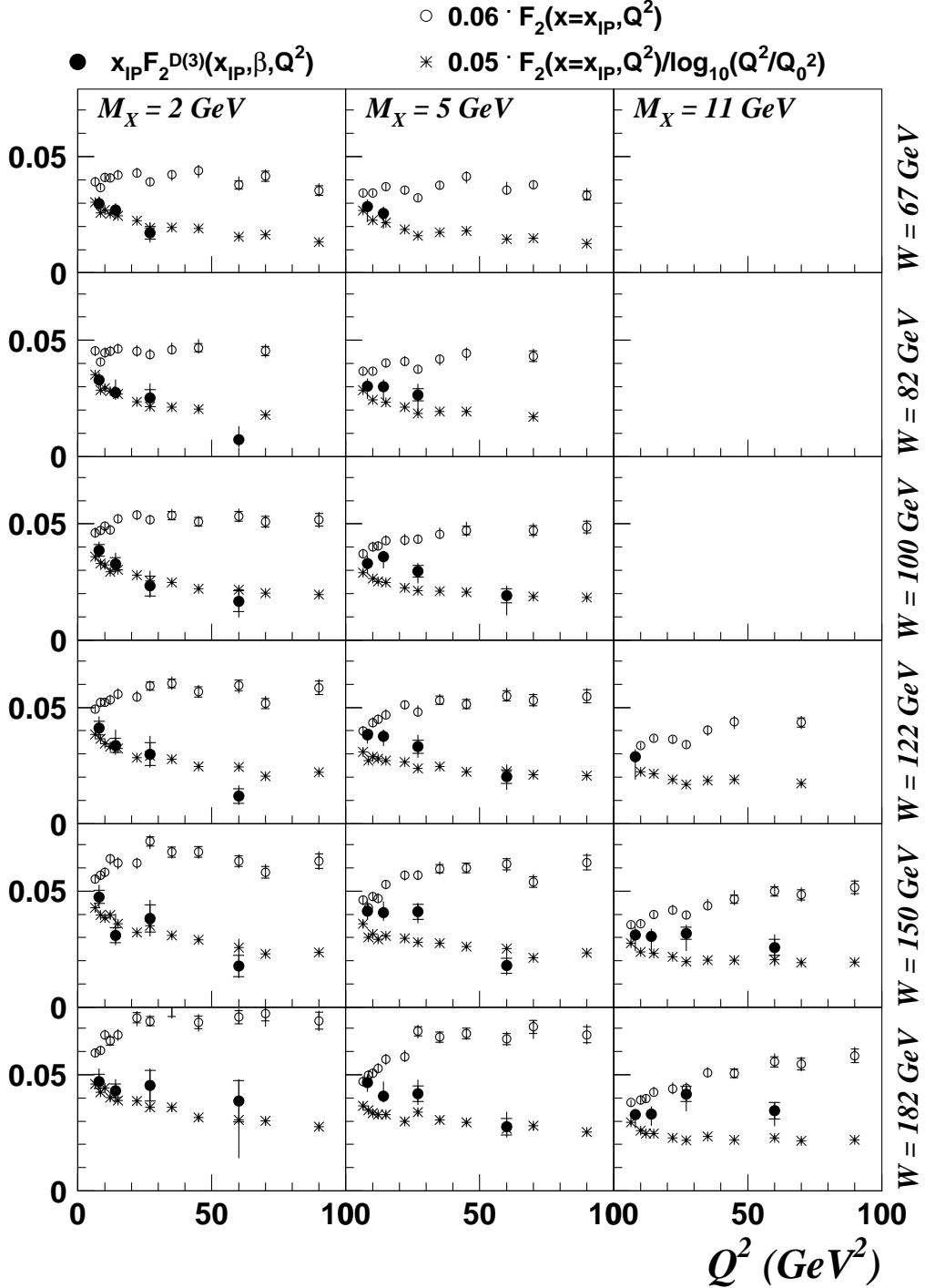


Figure 12: The solid points show the diffractive structure function for $\gamma^*p \rightarrow XN$, $M_N < 5.5$ GeV, multiplied by x_P , $x_P F_2^{D(3)}(x_P, \beta, Q^2)$, from this analysis, as a function of Q^2 for the (M_X, W) values indicated. The inner error bars show the statistical errors and the full bars the statistical and systematic errors added in quadrature. The open points show the structure function $F_2(x = x_P, Q^2)$ multiplied by 0.06 obtained with the 1994 data [19] as a function of Q^2 for the (M_X, Q^2) values indicated. The points marked by stars show $F_2(x = x_P, Q^2)/\log_{10}(Q^2/Q_0^2)$ scaled by a factor 0.05. Note that x_P is known when M_X, W and Q^2 are given.

ZEUS 1994

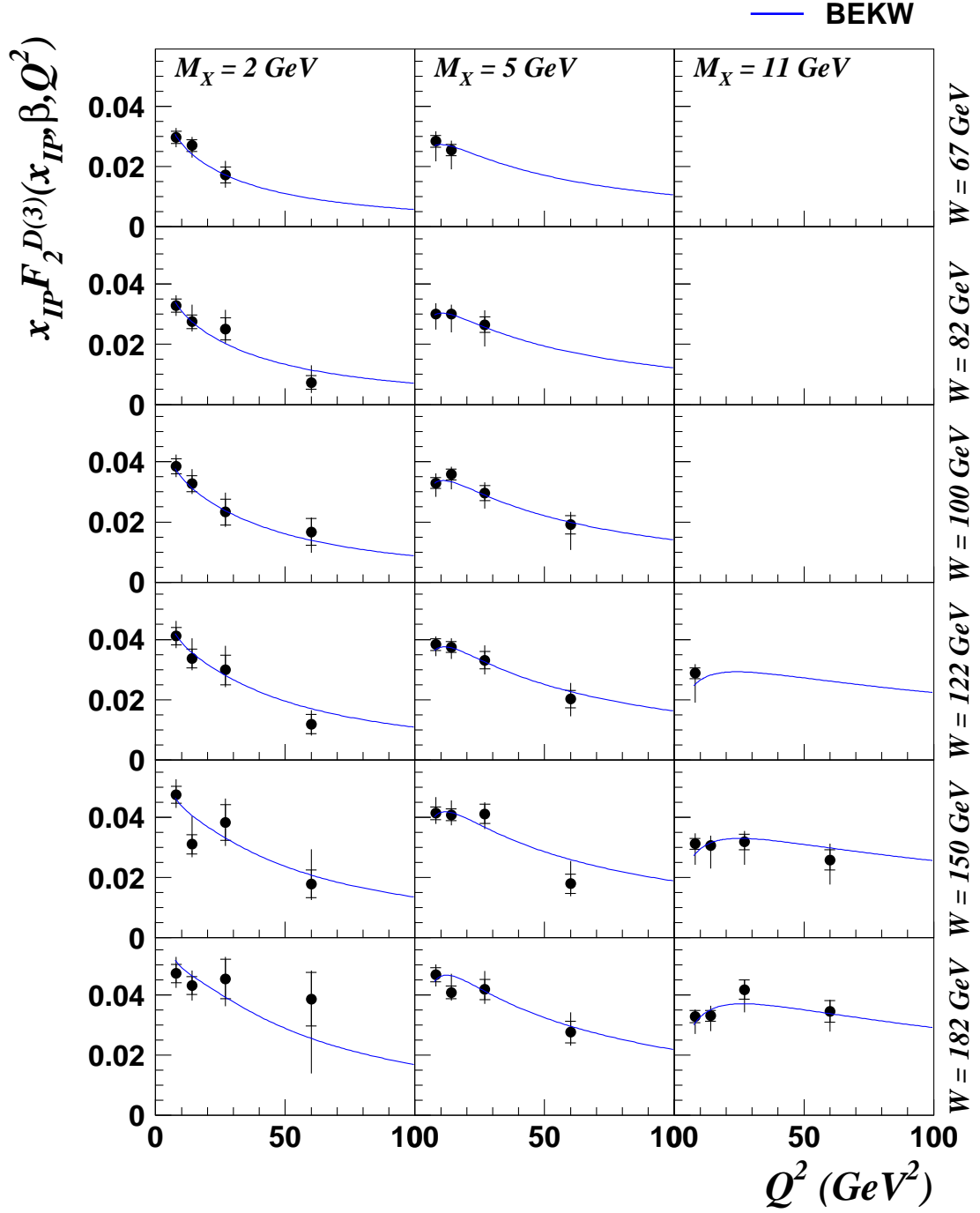


Figure 13: The diffractive structure function of the proton for $\gamma^*p \rightarrow XN$, $M_N < 5.5 \text{ GeV}$, multiplied by x_P , $x_P F_2^{D(3)}(x_P, \beta, Q^2)$, as a function of Q^2 from this analysis. The inner error bars show the statistical errors and the full bars the statistical and systematic errors added in quadrature. The curves show the fit results obtained with the BEKW model.

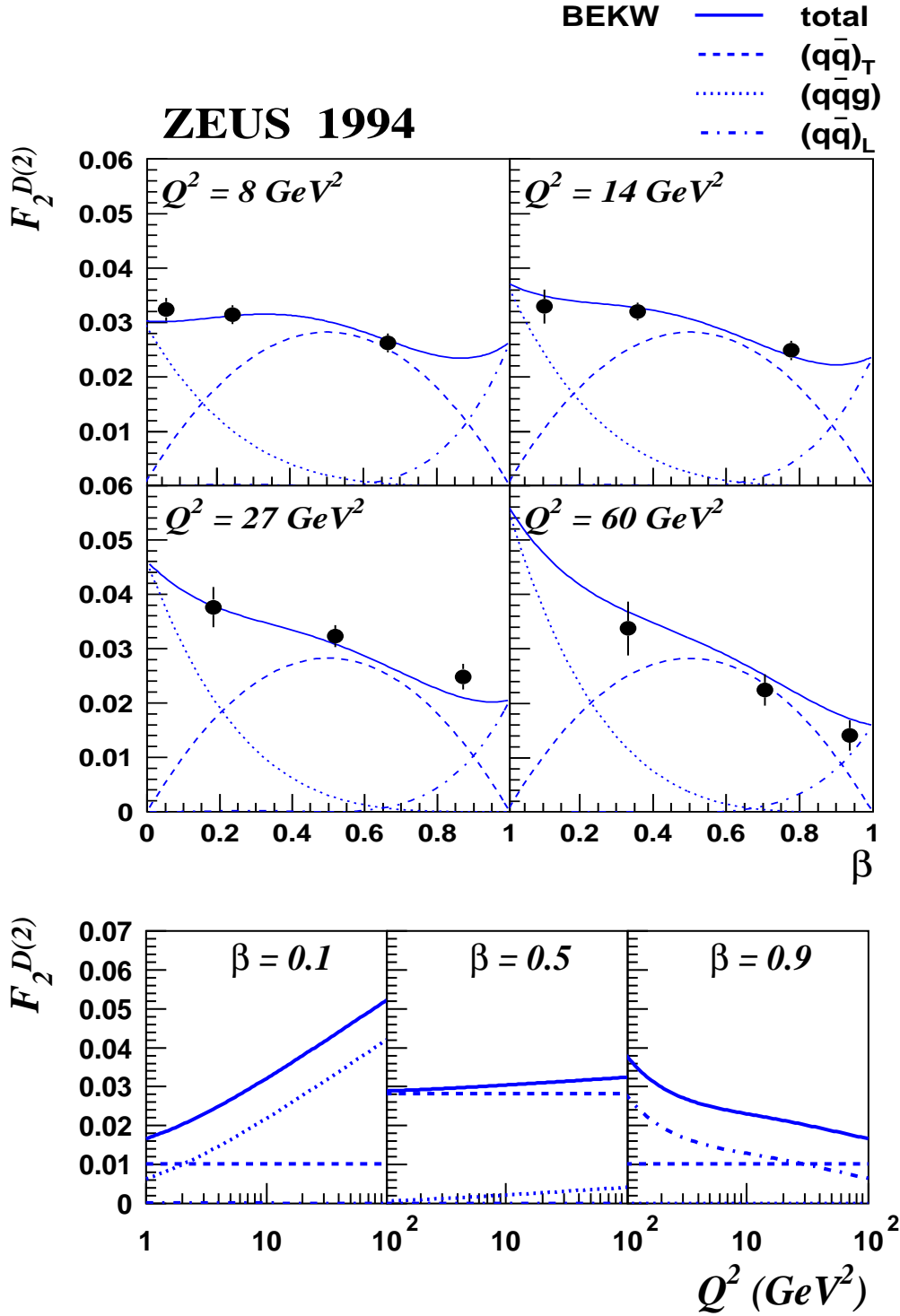


Figure 14: Top: The three components $(q\bar{q})_T$, $(q\bar{q}g)$ and $(q\bar{q})_L$ of the BEKW model building up the diffractive structure function of the proton and their sum $F_2^{D(2)}(\beta, Q^2)$ as a function of β for $Q^2 = 8, 14, 27$ and 60 GeV^2 , as obtained from a fit of the BEKW model to the data. Bottom: the same quantities as a function of Q^2 for $\beta = 0.1, 0.5$ and 0.9 .